Characterizing Structural Neural Networks

In Major Depressive Disorder using Diffusion Tensor Imaging

A Dissertation
Presented to
The Academic Faculty

by

Ki Sueng Choi

In Partial Fulfillment
of the Requirements for the Degree
Doctor of Philosophy in the
School of Bioengineering

Georgia Institute of Technology
December 2013

Characterizing Structural Neural Networks

In Major Depressive Disorder using Diffusion Tensor Imaging

Approved by:

Dr. Xiaoping Hu, Advisor
School of Biomedical Engineering
Georgia Institute of Technology

Dr. Paul Holtzheimer
Departments of Psychiatry and Surgery
Dartmouth College

Dr. Helen S. Mayberg
Department of Psychiatry and Neurology
Emory University

Dr. Robert Gross
School of Biomedical Engineering
Georgia Institute of Technology

Dr. Shella Keilholz
School of Biomedical Engineering
Georgia Institute of Technology

Dr. Xiaoming Huo
School of Industrial and Systems Engineering
Georgia Institute of Technology

Date Approved: September 13, 2013

TABLE OF CONTENTS

Contents	Pages
LIST OF TABLES	i
LIST OF FIGURES	ii
LIST OF ABBREVIATIONS	vii
SUMMARY	x
CHAPTER 1: INTRODUCTION	1
1.1. Statement of Thesis	1
1.1.1. White Matter Integrity in Major Depressive Disorder (Chapter 2)	2
1.1.2. White Matter Structural Networks in Major Depressive Disorder (Chapter 3)	3
1.1.3. Defining critical WM Pathways Mediating SCC DBS for TRD (Chapter 4)	3
1.2. Diffusion MRI	4
1.3. Diffusion Tensor Imaging	5
1.4. Major Depressive Disorder	8
1.5. WM integrity analysis in MDD using DTI	9
1.6. WM network analysis in MDD using DTI	10
1.7. Deep Brain Stimulation	12
1.8. SCC WM DBS for TRD	12
1.9. Modeling Activated Volume for DBS (VAT)	14

CHAPTER 2: White matter integrity in major depressive disorder 16

2.1. Introduction 16

2.2 Methods 19

2.2.1. Participants 19

2.2.2. Data Acquisition 20

2.2.3. Data Preprocessing 21

2.2.4. Fractional anisotropy map 22

2.2.5. Study specific fractional anisotropy template 22

2.2.6. DTI data analysis 25

2.2.6.1. Voxel-Based Morphometry 25

2.2.6.2. Track-Based Spatial Statistics 25

2.2.6.3. Voxel-wise FA analysis with MDDs and healthy controls 26

2.3. Results 27

2.3.1. Voxel-wise FA analysis using VBM and TBSS 27

2.4. Discussion and Conclusion 28

CHAPTER 3: White matter structural networks in Major Depressive Disorder 32

3.1. Introduction 33

3.2. Methods 34

3.2.1. Participants 34

3.2.2. Image pre-processing 34

3.2.3. Interface region of interest extraction for network analysis 35

3.2.4. Construction of structural connectivity network 38

3.2.5. Threshold for binary network based on network density 40

3.2.6. Network analysis 40

3.2.6.1. Random networks 41

3.2.6.2. Regular networks 41

3.2.6.3. Network degree 41

3.2.6.4. Characteristic path length 42

3.2.6.5. Clustering Coefficient 42

3.2.6.6. Global efficiency 43

3.2.6.7. Local efficiency 43

3.2.6.8. Small-worldness index 44

3.2.6.9. Nodal betweenness centrality 45

3.2.6.10. Area under curve for each network measures 45

3.2.7. Statistical analysis 46

3.3. Results 46

3.3.1. Small-world structural network 46

3.3.2. Alteration of global characteristics in MDD 50

3.3.3. Alteration of regional nodal characteristics in MDD 50

3.4. Discussions and Conclusion 52

CHAPTER 4: Defining critical WM Pathways Mediating Successful Subcallosal Cingulate Deep Brain Stimulation for Treatment-Resistant Depression 56

4.1. Introduction 57

4.2. Materials and Methods 63

4.2.1. Participants and clinical protocol 63

4.2.2. Magnetic resonance and computer tomography imaging 65

4.2.3. DBS Activation Volumes 66

4.2.4. Tract Map Generation using Individual VAT seeds 67

4.2.4.1. Preprocessing 67

4.2.4.2. Probabilistic Tractography 68

4.2.5 Anatomical active stimulation coordinates 72

4.3. Results 72

4.3.1. Probabilistic Tractography Analysis 72

4.3.2. Anatomical active stimulation coordinate 76

4.4. Discussion 78

CHAPTER 5: Conclusions and future directions 82

5.1 Problem Statement 82

5.2 Overview of Findings 82

5.3 Future Directions 83

References 89

LIST OF TABLES

Table 1. Summary of diffusion tensor imaging studies in patients with major depressive disorder using corrected whole-brain analysis 18

Table 2. Demographic and clinical characteristics of participants 20

Table 3. Extracted anatomical region of interest labels 37

Table 4. Brain regions showing abnormal nodal centrality in MDD compared with healthy control group 51

Table 5. Demographic and Clinical Characteristics 64

Table 6. Seed-to-Target Analysis: Normalized structural connectivity from bilateral activation volumes to six predefined regions of interest based on the Whole- Brain Connectivity maps. 75

Table 7. Coordinates of Activation Volumes in MNI space 77

LIST OF FIGURES

Figure 1. Illustration of water molecule diffusion, left: low restriction (isotropic), right: high restriction (Anisotropy) 6

Figure 2. Human SCC WM connectivity. A) Blue voxels identify the seed region for SCC WM tractography. B) Population-based mean tractography maps indicate voxels (blue) common to at least 75% of subjects. (David Gutman, Helen Mayberg, at el.) (14) 14

Figure 3. Axonal activation. A) Iso-potential contour lines of DBS voltage. B) DBS-induced extracellular potentials (Ve) interpolated onto an axon model. With sufficient polarization, action potentials initiate in the axon where ∂2Ve/∂x2 is largest (red trace) and propagate in both directions, C) calculated volume of Activated Tissue. (Cameron McIntyre, at el.) (81, 82). 15

Figure 4. A study specific fractional anisotropic template from 188 subjects. 24

Figure 5. The right genu of the corpus callosum was seen in a) seven of the eight "false positive" VBM results and b) eight of ten "false positive" TBSS results 28

Figure 6. Eighty-four cortical and subcortical WM/GM interface regions of interests for the brain network analysis (see Table 3 for detail region index) 36

Figure 7. A flowchart for the construction of the WM network by DTI, 1) Parcellate of T1-weighted structural MRI, 2) The reconstruction of all of the WM fibers in the whole brain using probabilistic tractography, 3) The binary networks of each subject were

created by threshold along network density, 4) The nodes and connections were mapped onto cortical surface. 39

Figure 8. Mean small-worldness index of all participants as a function of network density (cost). Small-world networks often have S >> 1 and it suggests that structural brain networks show small-world properties. 48

Figure 9. Small-world properties (clustering coefficient and characteristic path length) of structural brain networks. Red: MDD group, Blue: control group, Black: random network matched to all participants. Structural brain networks of both MDD and control group show higher cluster coefficient and equal characteristic path length compared with random networks. It is typical feature of small-world network. 48

Figure 10. The local efficiency of random, regular and structural WM brain networks as a function of network density. The brain networks under 5% ~ 60% network density showed higher local efficiency than matched random networks. 49

Figure 11. The global efficiency of random, regular and structural WM brain networks as a function of network density. The brain networks under each network density value showed higher global efficiency than matched regular networks. 49

Figure 12. Brain regions showing abnormal nodal centrality in brain structural networks (See table 4 for detail). Red: MDD < Control, Blue: MDD > Control, intensity: one or two centrality measure overlapped. 51

Figure 13. Anatomical location based the standardized method for targeting the SCG. A: Sagittal section showing the SCG. (Panels B and C are magnified images that correspond to the square in A.) B and C: To target the SCG, a line is initially traced parallel to the base of the Fr. Thereafter, AC-CCa and CCi-Fr lines are to be drawn parallel and

perpendicular to the base of the frontal lobe, respectively, and divided into quartiles. D: Axial and/or coronal planes of a region corresponding to 70–75% in AC-CCa and 25–30% in CCi-Fr should then be selected to define the anatomical gray/white matter junction of the SCG. SCG: subcallosal cingulate gyrus, AC: anterior commissure, CC: corpus callosum, CCa: anterior aspect of the CC, CCi: inferior portion of the CC, Fr: Frontal lobe (Hamani, Mayberg et al. (163)). 59

Figure 14. Demonstration of small anatomical location change cause different tract connections. A) Coronal image of the DBS electrode location. Inset shows the St Jude four contact electrodes and the respective contact numbers. Stimulation through contact 3 resulted in the best clinical outcomes. B) Sagittal view of the DBS electrode location. Note that the MRI background image is 3 mm behind the tip of the DBS electrode as not to obscure the tractography results which project in 3D around the electrode. C) White streamlines represent axon model trajectories passing by the DBS electrode. D) Voltage distribution imposed upon each axon model from stimulation at contact 3. E) Axon models (red streamlines) directly activated by therapeutic stimulation. F) Axon models directly activated by non-therapeutic stimulation. (Lujan, Choi, Mayberg et al. (190)) 62

Figure 15. Identification of contact location, a: post-surgical CT image overlapped onto pre-surgical T1 image for one subject. Contacts are numbered inferior to superior, 1 to 4. b: Activation volume using contact 1 and typical parameters for a sample subject (130Hz, 90us, 6mA), c: Probabilistic tractography connection from calculated activated volume for one subject. 67

Figure 16. Target regions used for DBS seed-to-target fiber probabilistic tractography maps. Three regions selected from Desikan and Harvard-Oxford atlases: medial frontal

cortex, anterior cingulate, and subcortical cluster (Basal ganglia including nucleus accumbens, caudate, putamen, and thalamus). Right and Left sided regions are sampled independently. 71

Figure 17. Group Whole-brain probabilistic tractography map defining the optimal DBS fiber tract target. Based on individual activation volume tract maps, all 6-month Responders (Blue) share bilateral pathways to: medial frontal-cortex (BA10) via forceps minor; subgenual, rostral and dorsal anterior cingulate via the cingulum bundle; and to nucleus accumbens, caudate, hypothalamus and anterior thalamus. Common tracts shared by all subjects regardless of 6-month response are shown in green. Abbreviations: mF: medial frontal, nAc: nucleus accumbens, Th: thalamus, Cau: caudate. 73

Figure 18. Whole brain fiber probabilistic tractography shared pathways map of more than 50% subjects, Responder group (Blue) shows robust shared pathways to medial frontal and subcortical regions. Green shows the shared pathways of all subjects which include responders and non-responders. Specific shared pathways to bilateral medial frontal were still indentified in responders group. 73

Figure 19. Anatomical location in MNI space of the VAT for responders (Blue) and non-responders (Red) at six months of chronic DBS. There is no differences in anatomical location between the responder and non-responder groups. 77

Figure 20. Qualitative DTI target selection using deterministic tractography, Top: Applied restricted (<35 degree) angular threshold for tracking, Bottom: < 90 degree angular threshold for tracking. 86

Figure 21. Preliminary result for quantitative DTI target selection using probabilistic tractography, Red arrow indicated the voxel has highest normalized connectivity value to six indentified key tracts. 87

LIST OF ABBREVIATIONS

AC	Anterior Commissure
ACC	Anterior Cingulate Cortex
AD	Axial Diffusivity
A-P	Anterior to Posterior
AUC	Area Under Curve
BC	Betweenness Centrality
BP	Bipolar depression
CC	Corpus Callosum
CCa	Anterior aspect of the CC
CCi	Inferior portion of the CC
CG25	Subgenual Anterior Cingulated cortex
CPL	Characteristic Path Length
CSF	Cerebrospinal Fluid
CT	Computed tomography
dACC	Dorsal Anterior Cingulate Cortex
DBS	Deep Brain Stimulation
DMN	Default Mode Network
DTI	Diffusion Tensor Imaging

DLPFC	Dorsolateral Prefrontal Cortex
D	Diffusion constant
DSM-IV	Diagnostic and Statistical Manual of Mental Disorders, Fourth Edition
EPI	Echo-Planer Imaging
FA	Fractional Anisotropy
Fr	Frontal lobe
FWHM	Full Width Half Maximum
GM	Gray Matter
HC	Healthy Control
HDRS	Hamilton Depression Rating Scale
Hz	Hertz
IPC	Inferior Parietal Cortex
MD	Mean Diffusivity
MDD	Major Depressive Disorder
MNI	Montreal Neurological Institute
MPRAGE	Magnetization-Prepared Rapid Gradient-Echo
MR	Magnetic resonance
MRI	Magnetic resonance imaging
NCD	Normalized Connectivity Density
OCD	Obsessive-Compulsive Disorder
P-A	Posterior to Anterior
PET	Positron Emission Tomography
rACC	Rostal Anterior Cingulate Cortex

RD	Radial Diffusivity
RF	Radio frequency
ROI	Regions of interest
SC	Structural Connectivity
SCC	Subcallosal Cingulate Cortex
SCG	Subcallosal Cingulate Gyrus
S. D.	Standard Deviation
SE	Spin echo
SPM	Statistical Parametric Mapping
SW	Small-Worldness
T	Tesla
TBSS	Tract-Based Spatial Statistics
TE	Echo Time
TFCE-FEW	Threshold-Free Cluster Enhancement Family-Wise Error-Rate
TI	Inversion Time
TR	Repetition Time
TRD	Treatment-Resistance Depression
UP	Unipolar Depression
VBM	Voxel-Based Morphometry
WM	White Matter

SUMMARY

Diffusion tensor imaging (DTI) is a noninvasive MRI technique used to assess white matter (WM) integrity, fiber orientation, and structural connectivity (SC) using water diffusion properties. DTI techniques are rapidly evolving and are now having a dramatic effect on depression research. Major depressive disorder (MDD) is highly prevalent and a leading cause of worldwide disability. Despite decades of research, the neurobiology of MDD remains poorly understood. MDD is increasingly viewed as a disorder of neural circuitry in which a network of brain regions involved in mood regulation is dysfunctional. In an effort to better understand the neurobiology of MDD and develop more effective treatments, much research has focused on delineating the structure of this mood regulation network. Although many studies have focused on the structural connectivity of the mood regulation network, findings using DTI are highly variable, likely due to many technical and analytical limitations. Further, structural connectivity pattern analyses have not been adequately utilized in specific clinical contexts where they would likely have high relevance, e.g., the use of white matter deep brain stimulation (DBS) as an investigational treatment for depression.

In this dissertation, we performed a comprehensive analysis of structural WM integrity in a large sample of depressed patients and demonstrated that disruption of WM does not play a major role in the neurobiology of MDD. Using graph theory analysis to assess organization of neural network, we elucidated the importance of the WM network in MDD. As an extension of this WM network analysis, we identified the necessary and

sufficient WM tracts (circuit) that mediate the response of subcallosal cingulate cortex DBS treatment for depression; this work showed that such analyses may be useful in prospective target selection. Collectively, these findings contribute to better understanding of depression as a neural network disorder and possibly will improve efficacy of SCC DBS.

CHAPTER 1

INTRODUCTION

1.1. Statement of Thesis

This dissertation seeks to characterize the structural organization of putative depression circuits using diffusion tensor imaging in an effort to aid future applications in optimizing surgical targeting for deep brain stimulation in treatment-resistant depressed patients. First, a comprehensive set of analyses of structural WM integrity was performed in a large sample of depressed patients to clarify and extend past observations of potential white matter abnormalities in MDD. Second, the topological organization of white matter connectivity was assessed using graph theory in order to elucidate potential structural connectivity differences in MDD patients versus controls. Finally, an analysis was performed to identify the key WM pathways impacted with successful subcallosal cingulate deep brain stimulation for treatment-resistant depression. These findings and methods will lead to better characterization of the neural circuitry in depression and will help to optimize pre-surgical targeting for SCC DBS.

1.1.1. White Matter Integrity in Major Depressive Disorder (Chapter 2)

Numerous DTI studies have looked for WM integrity differences in patients with MDD. However, the findings have been highly variable with respect to the location and direction of the difference in diffusion measurements such as FA, RD, MD, and AD. The source of this heterogeneity is unclear, but may reflect clinical heterogeneity between studies, small samples (and publication bias), and/or the use of suboptimal acquisition/preprocessing/analytic methods. ***The working hypothesis is that investigating WM integrity differences by voxel-wise analysis in large sample, optimized preprocessing (susceptibility correction, study specific template) and well-established analytical method (TBSS, VBM) will demonstrate the differences of WM integrity between MDD and healthy controls.*** In order to validate the WM integrity differences, voxel-wise cross-participant statistics were performed on both VBM and TBSS analysis with rigorous thresholds. Three different FA comparisons were assessed: (1) between 54 healthy controls and 134 MDD patients, (2) between 54 healthy controls and 54 age- and gender-matched MDD, (3) 100 iterative comparisons between 20 controls and 20 MDD patients, randomly selected from the larger sample; this last analysis was to identify the frequency of finding a "positive" statistical difference between the groups, using optimal analytic methods, with a sample size similar to those in previous studies.

1.1.2. White Matter Structural Networks in Major Depressive Disorder (Chapter 3)

White matter connections, which play a crucial role in coordination of information flow between different regions of gray matter, are important to understand pathological conditions in MDD. Focal WM disruption associated with depression has been reported in many previous studies (1-11), but little is known about the alternations in the coordinated patterns of WM networks in MDD. Network analysis, including structural connectivity analyses with graph theory, may be more likely to identify WM disruptions in MDD rather than WM integrity analysis. ***The working hypothesis is that assessing WM topological organization differences by structural connectivity and graph theory analysis will help to understand how the WM network changes associated with MDD.*** To assess disrupted WM topological organization in MDD, structural connectivity with probabilistic tractogrphy and graph theory analysis were used to compare the WM network differences between MDD and healthy control group.

1.1.3. Defining critical WM Pathways Mediating SCC DBS for TRD (Chapter 4)

SCC DBS has shown encouraging clinical results for treatment of treatment resistant depression (12). Anatomical tracing of white matter tracts in nonhuman primates and diffusion tensor tractography in humans suggest that therapeutic effects of SCC DBS may depend on stimulation of a specific combination of WM tracts (13, 14). However, specific fiber bundles and pathways critical for the antidepressant effect of SCC DBS

have yet to be defined. Furthermore, stimulation of a suboptimal location results in incomplete antidepressant effects (15). ***The working hypothesis is that the structural connectivity pattern analysis based on current active stimulation locations of SCC DBS will identify the white matter tracts that must be impacted by SCC DBS to generate optimal clinical response.*** This will be tested by the following three analyses: (1) define necessary and sufficient pathways using tractography from actual stimulation location within clinical responders, (2) validate findings with quantitative SC analysis, (3) assess the relationship between key pathways and clinical outcomes.

1.2. Diffusion MRI

The use of Magnetic Resonance Imaging (MRI) for disease diagnosis and monitoring has rapidly evolved as a non-invasive, high resolution imaging modality. One of the advanced techniques of MRI is diffusion imaging (16-18). Diffusion imaging has enormous potential for addressing research questions in both basic and clinical neuroscience. With its non-invasive nature and high sensitivity to measure white matter (WM) integrity, diffusion imaging has significantly influenced the field of neuroscience, and this technique has the potential to identify clinically significant biomarkers (19-22).

Diffusion, defined as the random Brownian motion of water molecules, describes the transportation of water molecules from one spatial location to other locations over

time. Diffusion MRI utilizes this random displacement of water molecules in biological tissue. In free medium tissue, such as cerebral spinal fluid (CSF), the measured diffusion movement is largely independent of the orientation of tissue (i.e., isotropic). In contrast, diffusion movement of water molecule in WM, where the diffusion of water molecules hindered by cellular membrane or architecture, the measured diffusion displacement is depends on the orientation of tissue (i.e., anisotropic). (17, 18, 20, 23). By applying a pair of diffusion sensitized gradients, the difference of diffusion properties (i.e., displacement of water molecule in certain tissue) between different tissues can be measure from image contrast.

1.3. Diffusion Tensor Imaging

Diffusion tensor imaging (DTI) is commonly used to assess WM integrity, fiber orientation, and WM connectivity using water diffusion properties. The diffusion tensor model is developed to characterize diffusion anisotropy in voxels because the anisotropy can't be represented by a single value due to its directional dependence. A three-dimensional principal eigenvectors and eigenvalues are derived from tensor model and these indicate the principal diffusion directions and associated diffusivity magnitudes along them, respectively. In the tensor model, it is assumed that a water molecule undergoing diffusion for a limited time will generally be constrained to a volume known as the diffusion ellipsoid. This volume is spherical in voxels with isotropic diffusion. In

contrast, voxels with anisotropic diffusion have oblate or prolate diffusion ellipsoids, depending on the relative magnitudes of the eigenvalues (Figure 1).

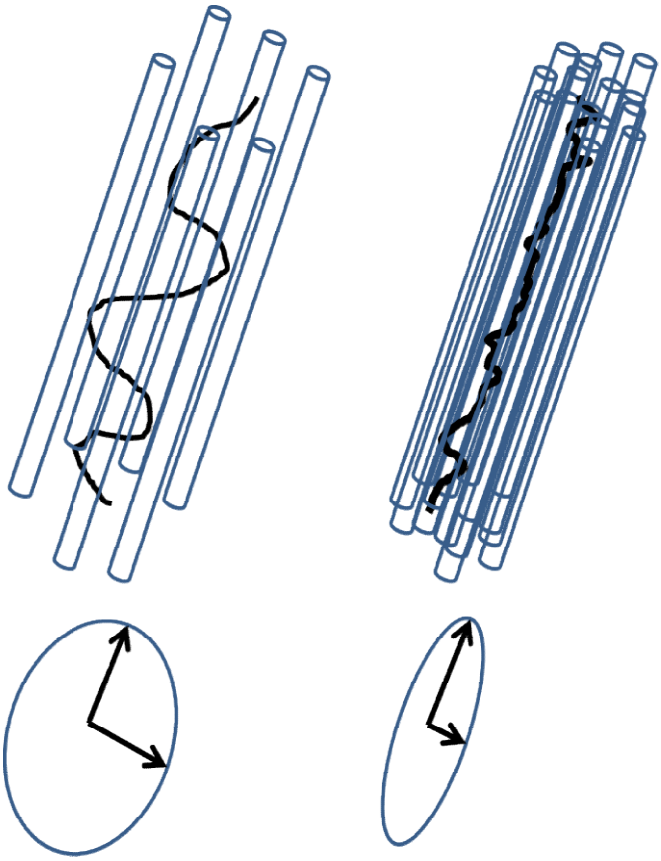

Figure 1. Illustration of water molecule diffusion, left: low restriction (isotropic), right: high restriction (Anisotropy)

Based on the concept of anisotropic water diffusion across tissue, DTI allows the characterization of the axonal architecture of WM by various diffusion tensor measurements. Diffusion tensor measurements reflects the degree of diffusion

directionality because diffusion perpendicular to main fiber direction is more hindered by myelin layers and cell membranes than diffusion along the main direction (17, 24). The most commonly used diffusion measurement is fractional anisotropy (FA). FA is highly sensitive to microstructural changes and has been reported a 20% reduction in demyelinated mice due to lose of myelin (25). In addition to FA, mean diffusivity (MD), radial diffusivity (RD), and axial diffusivity are frequently used for diffusion measurements. MD reflects the total magnitude of diffusion and higher MD has been reported with increased extra cellular bulk water in edema. RD appears to be modulated by myelin in white matter, where as axial diffusivity is more specific to axonal degeneration because it can measure disruption of axon (25).

In addition to various diffusion tensor measurements, anatomical connections in the brain can be measured by diffusion tractography method. Diffusion tractography is a method that follows fiber orientation estimates from point (voxel) to point (another voxel) to reconstruct the WM pathways (26). Diffusion tractography is the only available tool for measuring WM pathways or network non-invasively and in vivo. Such characterization of brain networks using tractography provides a comprehensive understanding of how these networks are structurally organized.

Due to high sensitivity and specificity of white matter structural change with in vivo, DTI has recently become a widespread methodology in brain research for several neuropsychiatric disorders such as depression, obsessive-compulsive disorder, Alzheimer's dementia, post-traumatic stress disorder, and addictive disorders (27, 28).

1.4. Major Depressive Disorder

Major depressive disorder (MDD) is a psychiatric disease characterized by a combination of symptoms that include a pervasive feeling of sadness, lowered energy, poor concentration and memory, and disruptions of sleep and appetite; patients with depression may also lose the ability to enjoy pleasurable activities, and they may have feelings of worthlessness and hopelessness that culminate in suicidal ideation and behaviors. MDD is a highly prevalent and a leading cause of worldwide disability (29). It affects approximately 1 in 6 people during their lifetime and causes significant occupational and social impairments (30).

Despite decades of research, the pathophysiology of MDD remains poorly understood. MDD is increasingly viewed as a disorder of neural circuitry in which a network of brain regions involved in mood regulation is dysfunctional (31, 32). In an effort to better understand the neurobiology of MDD and develop more effective treatments, much research has focused on delineating the structure and function of this mood regulation network. Recent, structural and functional neuroimaging studies have reported impairments in MDD in emotional processing, memory, and executive function networks (33), as well as local functional and structural abnormalities (34), particularly in the subgenual anterior cingulate cortex (Cg25) (35), hippocampus (36), parahippocampal gyrus (37), medial prefrontal cortex (38), dorsolateral prefrontal cortex (DLPFC) (39), ventral striatum, and amygdale (40, 41). Findings from these studies of MDD are still not clear, likely limited by approaches that fail to capture the multivariate

structure of abnormalities associated with this complex disorder. Indeed, it is not well-established yet whether MDD disrupts the structural and functional brain networks.

1.5. WM integrity analysis in MDD using DTI

Regions of interest (ROIs) and voxel-based analyses have been commonly used to analyze structural differences in DTI data between groups or within subjects over time. ROI based analyses have the advantage of being hypothesis driven and less statistically constrained by control for multiple comparisons. However, ROI analyses can be biased due to manual and non-standardized selection of ROIs; and, any differences outside of the ROIs chosen would not be identified. Voxel based methods have the advantage of allowing whole brain analyses and can be fully automated. This eliminates investigator bias (e.g., from manual ROI selection).

Two common voxel-based approaches for DTI analyses include voxel-based morphometry (VBM: direct voxel comparison between two different groups) and track-based spatial statistics (TBSS). VBM of DTI data is a fully automated method that allows investigation of WM integrity in the whole brain, at each voxel (42, 43). TBSS is a newer analytic technique developed to reduce the alignment and smoothing problems that have been reported with VBM (44, 45). Both approaches have been used to assess for

differences in white matter integrity in a variety of psychiatric disorders including MDD (46-48).

1.6. WM network analysis in MDD using DTI

In the past decade, much research has focused on volumetric or regional WM abnormalities to understand the neurobiology of MDD but it is still poorly understood due to highly variable previous findings with respect to the location and direction of the difference in white matter change. Recent developments in brain network analysis have been rapidly translated to studies in depression from brain regions to network organization. Although many studies have focused on the function of a network (49-54), including functional connectivity between key brain regions (55-61), there are not many studies that have focused on the structural network in MDD. Investigation of the large-scale structural interconnectivity with previous findings provided by functional connectivity studies may lead to better understanding of how and where brain regions mutually communicate (62-66). Network analysis, including structural connectivity analyses with graph theory, e.g., those using various tractography approaches based on diffusion tensor data, may be more likely to identify such abnormalities. Therefore, investigation of disruption in structural connection between regions is, now, an important focus of research for depression.

Graph theoretical approaches to the analysis of complex networks that could provide a powerful new way of quantifying the brain's structural system. Graphs are consisted of nodes (corresponding to brain regions) and edges (corresponding to synapses or pathways). In other words, graphs can be simply described by a connection matrix with binary elements that represent the presence or absence of an edge between pairs of node. Nodes can interact through direct connections, or indirectly via paths composed of multiple edges. The efficacy of these indirect interactions, which indicates how much parallel information can potentially be exchanged over the network, depends on the path length. Graphs of brain networks can be quantitatively examined for node degrees (number of edge that connect a node), clustering coefficients (tendency to cluster nodes into tightly connected), path lengths (distances between node to another node), and nodal centrality (relatively high importance in the network) (67, 68).

Graph theory analyses in various psychiatric disorders revealed that the topological organization in WM networks can be disrupted under pathological conditions such as Alzheimer's disease (69), schizophrenia (70), and multiple sclerosis (71). However, there is no study has been reported depression related alterations of the topological organization of WM networks.

1.7. Deep Brain Stimulation

Deep brain stimulation (DBS) is a powerful clinical technology, positively impacting the lives of tens of thousands of patients worldwide. DBS has FDA approval for the treatment of Parkinson's disease (PD) (72), essential tremor (ET) (73), dystonia (74), obsessive-compulsive disorder (OCD) (75). In addition, numerous clinical trials are currently underway or recently completed to evaluate its efficacy for other disorders, most notably epilepsy (76) and treatment resistance depression (TRD) (12, 15, 77, 78). Recent study of subcallosal cingulate cortex (SCC) WM DBS demonstrates the long-term safety and antidepressant efficacy in TRD (15). Although the early clinical results are very encouraging, it remains unclear which white matter pathways are critical to these DBS effects; better characterizing these critical pathways using structural connectivity analysis and finding ideal target location based on these critical pathways should further improve the efficacy SCC DBS.

1.8. SCC WM DBS for TRD

A first step toward understanding the effects of SCC WM DBS is to characterize the pathways that pass through the region. Two diffusion tensor tractography studies have been performed to determine variability in connectivity in and around the SCC WM DBS surgical target region, as well as compare the structural connectivity pattern of the SCC

WM target (13, 14). The results showed that the SCC WM seed had consistent ipsilateral connections to the medial frontal cortex, the full extent of the anterior and posterior cingulate, medial temporal lobe, dorsal medial thalamus, hypothalamus, nucleus accumbens, and the dorsal brainstem (Figure 2). These studies suggest the possibility that therapeutic effects of SCC DBS may depend on stimulation of a specific combination of WM tracts. However, these studies were performed from putative small target region without any consideration of actual stimulation location (general SCC regions) and parameters (fixed size). This inaccurate seed selection for tractography without location and size of each subject might be misleading the connection pathway from SCC WM stimulation. In addition to inaccurate seed, these results don't tell us which tracts are directly stimulated by the electrode in the context of actual patient data, or how activation of specific pathways is probabilistically related to specific outcome measures. To answer to these questions, precise seed selection based on individual patient data and volume of activated tissue (VAT) which can estimate direct simulation region by stimulation parameters is required. The structural connectivity pattern analysis from estimated precise VAT seed will help to find key therapeutic pathways from direct stimulation of SCC WM DBS.

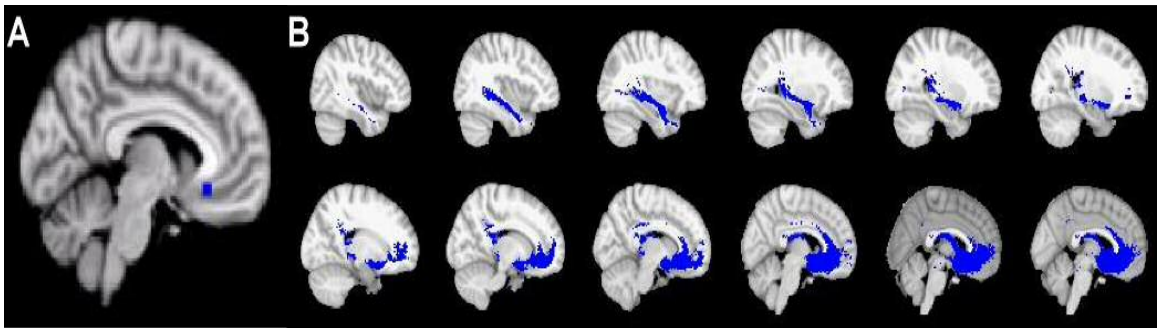

Figure 2. Human SCC WM connectivity. A) Blue voxels identify the seed region for SCC WM tractography. B) Population-based mean tractography maps indicate voxels (blue) common to at least 75% of subjects. (David Gutman, Helen Mayberg, at el.) (14)

1.9. Modeling Activated Volume for DBS (VAT)

DBS modulates neural activity with electric fields. The neural response to extracellular stimulation is related to the second spatial derivative of the extracellular potential distribution along a given neural process ($\partial 2Ve/\partial x2$) (79, 80). These modeling of neural response have been applied to predict the VAT for a given stimulation parameter setting in the context of diffusion tensor based DBS models (81, 82). The most important output of a diffusion tensor based DBS model is the predicted neural response to the stimulation. The biophysical model simulates the neural response to extracellular stimulation via multi-compartment cable models of neurons. The extracellular voltage distribution generated by the DBS electrode is applied to each compartment of the axon model, generating trans-membrane currents which if strong enough will elicit an action potential (Figure 3). This diffusion tensor DBS model will provide an exact shape of

VAT that is currently stimulated with several stimulation parameters such as amplitude, frequency, and pulse width. The optimized shape of VTA will, therefore, improve an accuracy of structural connectivity analysis because it will provide exact stimulated WM fibers for SCC WM DBS.

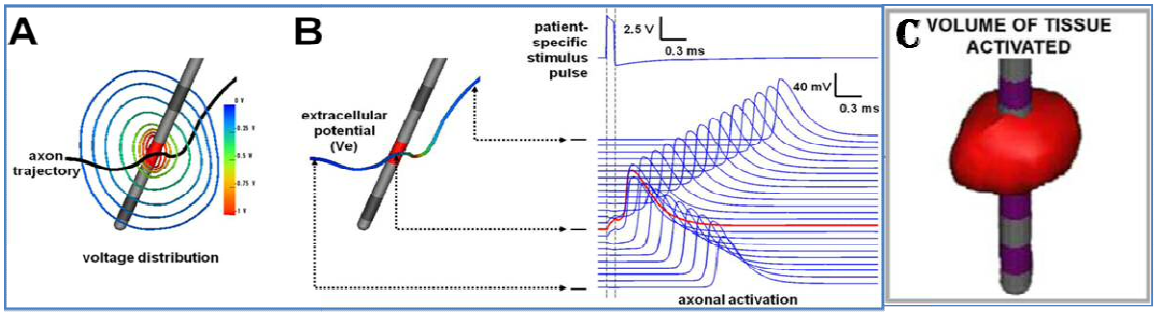

Figure 3. Axonal activation. A) Iso-potential contour lines of DBS voltage. B) DBS-induced extracellular potentials (Ve) interpolated onto an axon model. With sufficient polarization, action potentials initiate in the axon where $\partial 2Ve/\partial x2$ is largest (red trace) and propagate in both directions, C) calculated volume of Activated Tissue. (Cameron McIntyre, at el.) (81, 82).

CHAPTER 2

White matter integrity in major depressive disorder

The objective of this chapter is to investigate structural abnormality in major depressive disorder, including white matter integrity using diffusion tensor imaging. White matter fractional anisotropy, radial diffusivity, mean diffusivity, and axonal diffusivity are assessed to evaluate a major role of neurobiology in major depressive disorder with definitive analysis.

2.1. Introduction

Numerous DTI studies have looked for white matter integrity differences in patients with MDD (1-11). However, the findings have been highly variable with respect to the location and direction of the difference in FA (Table 1). Six studies report a reduction of FA (in various regions) in MDD patients compared to HC, while another five studies show either an increase or no difference in FA between the groups. The source of this heterogeneity is unclear, but may reflect clinical heterogeneity of different patient cohorts, small samples (and publication bias), and/or the use of suboptimal acquisition/analytic methods. Regarding the last possibility, interpretation and analysis of

DTI data may be complicated by a small number of diffusion weighted directions (more directions yield higher integrity data), anisotropic voxel size and susceptibility distortion.

In an effort to provide a more definitive analysis of potential white matter abnormalities in depressed patients, DTI was performed as part of a large study of depressed patients and in a group of healthy controls all scanned using a common protocol (83, 84). Using optimized processing methods, VBM and TBSS were performed on these data to assess for differences in FA between the groups. A strict threshold for statistical significance was applied.

Table 1. Summary of diffusion tensor imaging studies in patients with major depressive disorder using corrected whole-brain analysis

Study	Participants						Imaging parameters				Data Processing	Analysis Method	Findings after rigorous threshold	
	Healthy control			MDD										
	n	Age (Mean (S.D.))	Gender (M/F)	n	Age (Mean (S.D.))	Gender (M/F)	Magnet strength	DTI Resolution (mm)	Number of diffusion direction	Number of average			Reduction	Increase
Tha et al. (2013)	19	36.5(12.5)	13/6	19	38.6(14.5)	12/7	1.5T	1.875 * 1.875 * 5	12	2	No distortion correction Study specific template SPM	VBM	Bilateral frontal WM Anterior limbs of internal capsule Let putamen Right thalamus Bilateral cerebellar hemispheres	
Cole et al. (2012)	66	50.4(7.9)	23/43	66	48.6(8.2)	30/36	1.5T	2.5 * 2.5 * 2.5	60	1	No distortion correction JHU DTI template FSL	TBSS ROI regions	Splenium Genu and body of corpus callosum Bilateral superior longitudinal fassiculus anterior and posterior corona radiata Anterior and posterior limbs of internal	
Zhu et al. (2011)	25	20.33(1.68)	10/15	25	20.55(1.86)	10/15	1.5T	2 * 2 * 4	12	1	No distortion correction MNI template FSL	TBSS	Left anterior limb of internal capsule Right parahippocampa gyrus Left posterior cingulate cortex	
Wu et al. (2011)	21	30.4(8.2)	9/12	23	31.4(8.8)	10/13	1.5T	0.94 * 0.94 * 4	12	5	No distortion correction MNI template DTIStudio & SPM	VBM	Right superior longitudinal fassiculus Rihgt middle frontal Left inferior parietal	
Korgaonkar et al. (2010)	39	29.6(46.2)	18/21	29	40.5(15.8)	12/17	3.0T	1.72 * 1.72 * 2.5	42	1	No distortion correction MNI template FSL	TBSS	No difference between MDD Vs controls Reduction between meloncholic and controls in corpus callosum, dosalateral prefontal, thalamic projection fiber	
Abe et al. (2010)	42	48(13.2)	22/20	21	48.1(13.5)	11/10	1.5T	1.875 * 1.875 * 5	6	4	Image based distorion correction Study specific template FSL	VBM	No difference	
Kieseppa et al. (2010)	20	42(11.6)	10/10	16	48.4(10.3)	2/14	1.5T	1.75 * 1.75 * 5	12	1	No distortion correction MNI template FSL	TBSS	No difference	
Cullen et al. (2010)	14	16.81(1.5)	6/8	14	16.79(1.29)	4/10	3.0T	2 * 2 * 2	30	1	Field map distortion correction Study specific template FSL	TBSS	No difference	
Blood et al. (2010)	22	35.3(11.6)	10/12	22	36.3(12.1)	10/12	3.0T	2 * 2 * 2	6	6	No distortion correction MNI template FSL & Freesurfer	ROI regions	Dosallateral prefrontal cortex Left precentral gyrus	Ventral tefmental area Substantia nigra Right calcarine cortex
Zou et al. (2008)	45	31(10.3)	15/30	45	33.2(8.9)	15/30	3.0T	1.875 * 1.875 * 3	14	2	No distortion correction MNI template DTIStudio & SPM	VBM	Left anterior limb of internal capsule Left superior longitudinal fasciculus	
Ma et al. (2007)	14	27.1(6.7)	2/12	14	28.9(8)	2/12	1.5T	1.875 * 1.875 * 4	12	5	No distortion correction MNI template SPM	VBM	Right middle frontal gyrus Left lateral occipitotempolar gyrus Subgyral WM of the right parietal lobe Right angular gyrus	

TBSS: Track-Based Spatial Statistics, VBM: Voxel Based Morphometry. ROI: Region Of Interest, MNI: Montreal Neurological Institute, Dir.: Directions, Avg.: Average

2.2 Methods

2.2.1. Participants

Fifty-four healthy controls (HC) and one hundred thirty four MDD patients participated in accordance with Institutional Review Board policies at Emory University. HC participants were screened for history of current or past neurological and psychiatric disorders. These subjects were recruited as part of three separate imaging studies at Emory University using the identical DTI protocol. Eligible depressed patients were adult outpatients between 18 and 60 years of age who meet the Diagnostic and Statistical Manual of Mental Disorders, Fourth Edition (DSM-IV) criteria for a primary diagnosis of MDD without psychotic features. Patients were excluded if they met lifetime criteria for psychotic disorder, or currently met criteria for OCD. Medication free Patients with new onset, recurrent, or chronic MDD both with and without past treatment were enrolled. All patients were participating in one of two studies involving randomized treatment and imaging biomarkers. The 28-item Hamilton Depression Rating Scale (HDRS) was assessed before MR data are acquired. Table 2 shows the demographic information and clinical characteristics of all participants.

Table 2. Demographic and clinical characteristics of participants

		Health control (n = 54)	MDD (All n=134 Matched n = 54)	Statistics F or χ^2	df	p
All participants	Age (Years)	34.42(10.06)	38.49(11.09)	0.6	186	0.4
	Gender (Males/Females)	28 / 26	64 / 70	0.25	1	0.6
	HDRS Score		19.28(3.47)			
	Duration of Illness (Years)		9.34(10.38)			
Age & Gender Matched	Age (Years)	34.42(10.06)	34.41(8.9)	2.19	106	0.7
	Gender (Males/Females)	28 / 26	28 / 26	0	1	1
	HDRS Score		18.74(3.33)			
	Duration of Illness (Years)		7.77(8.41)			

Duration of Illness: Period from age of onset to recruitment for study, MDD: Major depressive disorder

2.2.2. Data Acquisition

Data were acquired on a 3T Tim Trio MRI scanner (Siemens Medical Solutions, Malvern, PA, USA) that permits maximum gradient amplitudes of 40mT/m. A twelve-channel head array coil was used. DTI and T_1-weighted data were collected within a single session for each subject and foam cushions were used to minimize head motion. A single-shot spin-echo echo-planar imaging (EPI) sequence was used with generalized auto-calibrating parallel acquisition (GRAPPA) with two fold acceleration (R=2) (85). The parameters used for DTI were: FOV = 256 x 256; b value = 1000 sec/mm^2; voxel resolution = 2×2×2 mm; number of slices = 64; matrix = 128 x 128; TR/TE = 11300/104ms; 60 non-collinear directions with four non-diffusion weighted images (b=0)

were acquired twice: once with phase encoding in the anterior to posterior (A-P) direction and once in the posterior to anterior (P-A) direction. To compensate susceptibility distortion, both phase up and down images were acquired. In addition to susceptibility distortion correction, we used slightly longer TR and TE than a typical diffusion protocol due to mechanical vibration of the patient table that caused by the low frequency gradient switching associated with the diffusion weighting. High-resolution T_1 images were collected using a 3D magnetization-prepared rapid gradient-echo (MPRAGE) sequence with following parameters: TR/TI/TE = 2600/1100/3 ms; voxel resolution = 1×1×1 mm; number of slices = 176; matrix = 224×256.

2.2.3. Data Preprocessing

Magnetic resonance imaging data were preprocessed using FSL software (www.fmrib.ox.ac.uk/fsl; Analysis Group, FMRIB, Oxford, United Kingdom (86). Non-brain regions of T_1 and diffusion weighted data (both A-P and P-A) were removed using the BET toolbox. To estimate and correct susceptibility induced distortion of the diffusion weighted images, a phase reversal distortion correction method, which also called Topup correction tool in FSL, was applied on obtained A-P and P-A diffusion data (87). This phase reversal distortion correction method assumes that different phase encoding diffusion images are caused by an identical magnitude of susceptibility distortion in the phase encoding direction, and can be resolved by estimating the underlying magnetic field map. By combining the images acquired in opposite phase

encoding directions, the distortion can then be corrected. To help confirm correction, deterministic and probabilistic tractography results of well-known brain white matter bundles are inspected for evidence of distortion.

2.2.4. Fractional anisotropy map

Fractional anisotropy, radial diffusivity, mean diffusivity, and axonal diffusivity maps were generated from phase reversal distortion corrected diffusion weighted data. To improve the signal-to-noise ratio of diffusion tensor fitting, four non-diffusion weighted images (b_0) are averaged after three of them are aligned to one reference image by affine transformation. Diffusion weighted image data were aligned to averaged non-diffusion weighted image by rigid body affine transformation to remove motion and eddy current induced artifact (88). Diffusion tensor, eigenvector and eigenvalue were then calculated by a tensor fitting model for quantification of directional diffusion and FA (Fdt function within FSL toolbox, Oxford, UK). (89).

2.2.5. Study specific fractional anisotropy template

A study specific FA template was created using all 188 subjects (MDD and control groups combined) to reduce misalignment error that caused by common brain template which is derived from specific age range (20~30) and healthy controls. First,

each subject's FA image was transformed to a standard FA template (FMRIB58_FA, http://www.fmrib.ox.ac.uk/fsl/data/FMRIB58_FA.html) using rigid body affine transformation (degree of freedom: 6, FLIRT, FSL) followed by Gaussian smoothing with 3 mm full width half maximum (FWHM) and then averaged across subjects to create the initial study specific FA template. A second FA template was created by performing a similar process, but using linear co-registration (degree of freedom: 12) to the first FA template map, followed by blurring with a 3mm FWHM Gaussian kernel. The final template was created by averaging across subjects (Figure 4). This process was iterated six times using non-linear image registration (FNIRT, FSL). Results were visually inspected after each iteration for quality control. For analyses, each subject's FA map was co-registered to the study specific template map by performing a linear (FLIRT, dof 12) transformation followed by a nonlinear (FNIRT) transformation. Individual subject FA transformation information to study specific FA template was saved and used for the other measurements (RD, MD, Axonal diffusivity) normalization.

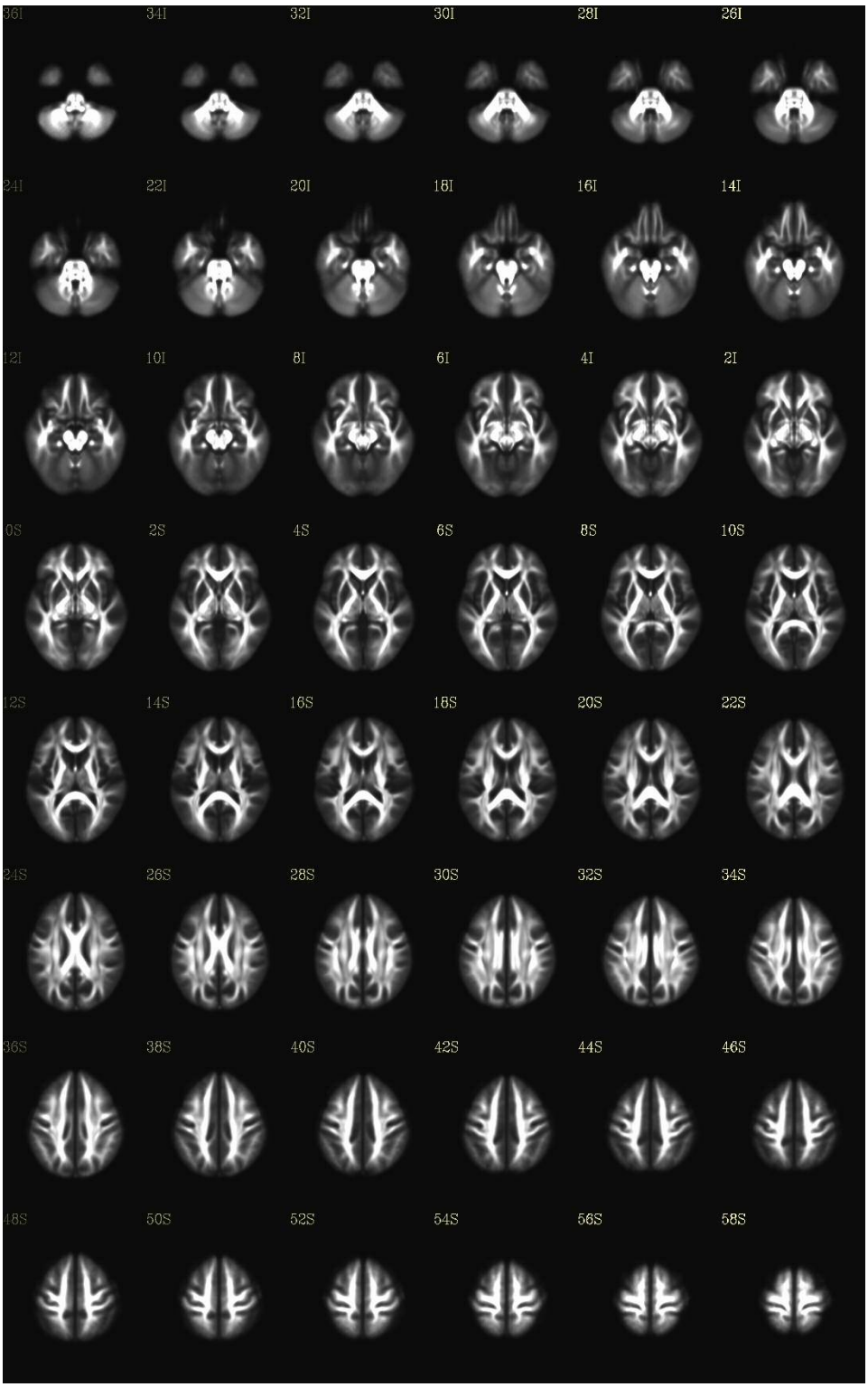

Figure 4. A study specific fractional anisotropic template from 188 subjects.

2.2.6. DTI data analysis

For statistical analysis, a permutation-based statistical inference test with threshold-free cluster enhancement (TFCE: enhancing cluster-like structures in an image without having to define an initial cluster-forming threshold or carry out a large amount of data smoothing), using neighborhood voxel information to improve statistical sensitivity. For multiple comparisons, a family-wise error (FWE) correction (corrected $p<0.05$, 10000 permutations) was used with estimation of cluster size (TFCE_FWE correction and randomize functions within FSL) (90).

2.2.6.1. Voxel-Based Morphometry

The normalized FA, RD, MD, and axonal diffusivity map for each subject was next smoothed using a 5 mm FWHM Gaussian isotropic kernel to remove possible error caused by anatomical mismatching of like-brain regions.

2.2.6.2. Track-Based Spatial Statistics

TBSS was performed using the same FA maps as used for the VBM analyses. For TBSS, the aligned FA maps were averaged to create a mean FA map. This mean FA map was then thinned to create a mean FA skeleton represent centers of tracts common to all subjects. FA values less than 0.2 were judged as noise and eliminated to reduce potential confounds introduced by inter-subject variability and partial volume effects (44, 45). The aligned and threshold FA map of each subject were lastly projected onto the

mean FA skeleton for the voxel-wise statistical analysis. Same processing steps were applied to RD, MD, and axonal diffusivity.

2.2.6.3. Voxel-wise FA analysis with MDDs and healthy controls

Voxel-wise cross-participant statistics were performed on both VBM and TBSS (skelectonized) analysis using TFCE-FWE. To remove age and duration of illness effect in statistical test, both age and duration of illness were used as covariate and statistical results were adjusted using general linear model. We performed two sets of FA (MD, RD, axonal diffusivity) comparisons: (1) between all fifty-four healthy controls and one hundred thirty four MDD patients; and (2) between an age and gender-matched subset (54 subjects per group) to account for any potential effects due to minor mean age and gender differences among the healthy controls and MDD patient group, (Table 2). In a post-hoc analysis, twenty subjects from each group were randomly selected and compared with both VBM and TBSS analysis; this was iterated 100 times using different subsamples – this post-hoc analysis was performed to assess for the "false positive" rate in our sample using samples sizes similar to previous analyses.

2.3. Results

2.3.1. Voxel-wise FA analysis using VBM and TBSS

Voxel-wise statistics adjusted for age and duration of illness revealed no significant differences in FA, MD, RD, and axonal diffusivity between MDD and HC group for either the VBM or TBSS analysis. With a gradual decrease in statistical threshold, significant FA differences began appearing in genu of corpus callosum with a p-value of 0.15 (TFCE-FWE corrected). In addition to full group comparisons, the voxel-wise statistical analysis of the age- and gender-matched subset also found no FA differences for either analysis.

With the 100 interactive FA analyses using 20 subjects/group selected randomly for each comparison, statistically significant FA differences were identified for ten of the TBSS comparisons and eight of the VBM comparisons ($p < 0.05$ TFCE-FWE corrected). The brain regions seen in these "false positive" results included a spatially diverse set of WM regions. Of note, the genu of the corpus callosum was seen in eight of the ten "false positive" TBSS results and seven of eight "false" positive VBM results (Figure 5).

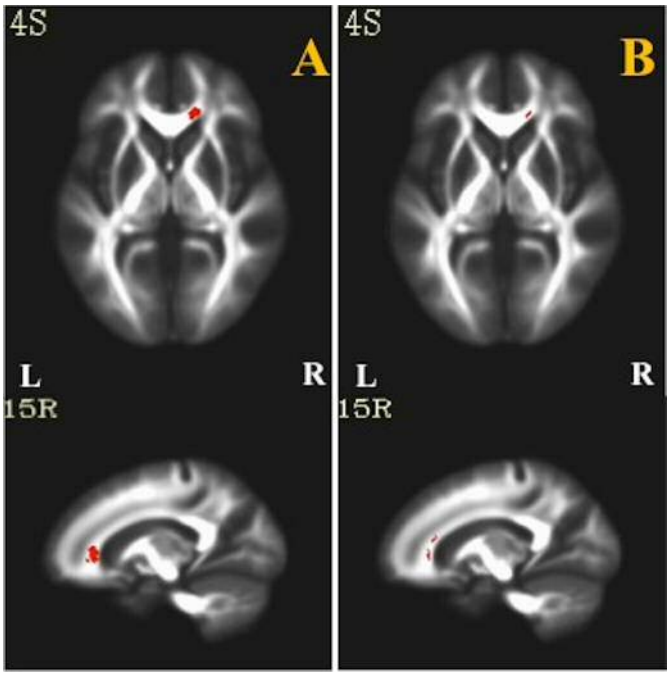

Figure 5. The right genu of the corpus callosum was seen in a) seven of the eight "false positive" VBM results and b) eight of ten "false positive" TBSS results

2.4. Discussion and Conclusion

Despite previous reports of FA abnormalities in depression, this large DTI study found no significant differences in FA (RD, MD, Axial diffusivity) between MDD patients and controls using either VBM or TBSS. This included analyses of a subset of age- and gender-matched subjects. In an exploratory analysis, differences in FA between the groups were only seen when the threshold was decreased to a relatively low level – and, even then, the findings appeared "noisy". Taken together, these results suggest that disrupted WM integrity does not play a major role in the neurobiology of MDD.

These findings are not entirely inconsistent with prior DTI studies in MDD. When reviewed *in toto* (Table 1), it is notable that previous studies differ significantly in which brain regions show FA abnormalities. In our post-hoc analysis, where a series of smaller, randomly selected subgroups of patients and controls were compared, about 10% of comparisons showed "positive" FA differences despite no differences in the full sample. Similar to the studies in Table 1, the subsample analyses showing FA differences varied considerably in which regions were identified. Interestingly, a region consistently identified as showing FA differences between MDD patients and controls in our post-hoc analysis was the genu of the corpus callosum – a region identified in the previously published reports (6, 10). Given with the well-known prefrontal distortion in DTI images, it is possible that this region is especially vulnerable to false positive findings in DTI analyses (91).

There are several strengths of this study that increase confidence in these findings. First, this would be the largest published DTI study to date comparing MDD patients and controls; therefore, these findings likely represent a better estimate, compared to smaller studies, of reliable differences in white matter integrity between MDD patients and controls. Second, a study specific DTI template was created using the full sample (n=188) with an iterative normalization method, such that errors due to co-registration were reduced. Third, a phase reversal distortion correction was applied to the diffusion weighted images to reduce errors related to well-known frontal distortion in DTI images due to the sinuses (91, 92). Very few of the past published studies have used such a correction that is now relatively standard. Fourth, we utilized the most up-to-date

analytic methods to reduce possible errors due to diffusion imaging acquisition and statistical comparison. For instance, four non-diffusion (b_0) images were acquired during each scan session, then manually averaged to improve signal to noise ratio. Sixty non-collinear diffusion directions and isotropic voxels were used to improve angular resolution and data integrity (anisotropic voxels in diffusion acquisition can affect tensor modeling and artificially alter FA values (93)). Finally, well-established diffusion analysis methods were used to calculate FA value, and a rigorous statistical threshold was applied.

Other possibilities exist for why previous reports have identified FA differences in MDD patients versus controls while this study did not. Samples selection differences may be a significant contributing factor, though subjects in this study were carefully evaluated to insure they met diagnostic eligibility criteria using structured diagnostic instruments and rating scales; it is therefore unlikely that they differed significantly from other MDD subjects enrolled in earlier studies. It is possible that subgroups of MDD patients (treatment-resistant, late-onset, early trauma exposure, familial, etc.) may be more likely to have white matter abnormalities, though this awaits verification. Notable in our analysis is that those contrasts showing positive differences couldn't be attributed to a randomization bias of the study source of either the MDD patients or the control subjects. In general, prior studies used acquisition and analytic methods that were not optimal compared to current standards. This could introduce bias into the analyses increasing the likelihood of a Type I error.

Although this study found no regional differences in FA between MDD patients and controls, this does not argue against the continued use of diffusion imaging to assess white matter in the study of MDD. Despite these negative findings in MDD, diffusion imaging remains a powerful tool in the study of neuropsychiatric disorders, particularly in light of oligodendroglia abnormalities in post mortem studies (94-96). As the field progresses, improved acquisition and analytic techniques may allow for the identification of white matter abnormalities between groups that are too subtle for current approaches to distinguish. Further, it may be that certain subgroups of depressed patients are more likely to show white matter abnormalities, such as patients with extreme treatment resistance or late-onset depression. Additionally, it may be that the pathophysiology of depression does not involve the integrity of white matter *per sé*, but rather abnormalities in the white matter connections between brain regions involved in mood regulation. To this end, structural connectivity analyses, e.g., those using various tractography approaches based on diffusion-weighted data, may be more likely to identify such abnormalities (97, 98).

CHAPTER 3

White matter structural networks in Major Depressive Disorder

In the previous chapter, multiple diffusion measurements, including fractional anisotropy, radial diffusivity, axonal diffusivity, and mean diffusivity, showed no statistical differences between health controls and MDD. These results suggest that disrupted white matter integrity does not play a major role in the neurobiology of major depressive disorder in this relatively large study using optimal imaging acquisition and analysis; however, this does not eliminate the possibility that the white matter connections between brain regions are involved in mood regulation.

Graph theory provides a powerful tool for quantifying the organization of brain connectivity, allowing the brain to be depicted as graphs. Several studies have reported the disrupted topological organization of WM network in various neuropsychiatric disorders. However, no study has reported depression-related alterations of the topological organization of WM networks. In this chapter, probabilistic tractography and graph theory analysis were used to investigate the topological organization of whole-brain WM networks in MDD.

3.1. Introduction

Recent developments in the quantitative analysis of brain connectivity, based largely on graph theory, have suggested that human whole-brain WM networks can be reconstructed by diffusion tractography (98-100), and graph theory in particular provides a framework for characterizing topological properties of brain network organization (101-105). In graph theory, the brain is represented as a graph composed of nodes (brain regions or voxels), and edges (structural and functional connections between the nodes). Using graph theory, the organization of normal brains can be described in a small-world fashion with a high level of local clustering (i.e. nodes are often highly connected to their neighbors), combined with shot path lengths (i.e. it takes fewer steps from one node to another node in this network compared to a random network) at low cost (i.e. the mean physiological distance between two connected nodes is considerably less than a random network) (106). By comparing groups, this powerful tool then allows for the measurement of the disruption of brain organizational patterns in various brain diseases such as Alzheimer's disease (107-109), schizophrenia (110-112), and depression (113-116).

Graph theory investigations of depressed individuals have been performed in small samples and limited to investigation of functional networks or gray matter volume. These studies have found brain network abnormalities in terms of path length and number of connections. WM networks have not been investigated with these methods.

In this study, quantitative global and regional topological organization of the brain were assessed, for the first time, using MR-derived structural connectivity of the whole-brain WM network using graph network analysis in a large sample of patients with MDD. The hypothesis is that, MDD patients would show 1) abnormal network topology, including significantly abnormal global and nodal efficiency; 2) lower centrality, including betweenness and degree centrality compared with healthy control subjects.

3.2. Methods

3.2.1. Participants

For this analysis, the same subjects were used as for chapter 2. Fifty-four healthy controls and 134 MDD patients were analyzed. Demographic and clinical characteristic information of participants are shown in (Table 2).

3.2.2. Image pre-processing

The same image pre-processing (acquisition) steps were applied as described in chapter 2. In addition to pre-processing, cortical and subcortical gray matter were segmented for region of interest extraction.

3.2.3. Interface region of interest extraction for network analysis

Structural connectivity calculated from gray matter (GM) seed to GM target has low fiber coherence and is not robust due to nature of diffusion contrast in GM. To improve robustness of probabilistic tractography and reduce error caused by GM seeds, white- and gray-matter interface regions were generated. Each individual's high resolution T_1-weighted image was parcellated to extract 84 cortical and subcortical (42 per hemisphere) regions of interests (ROIs), excluding brain stem and corpus callosum, using the FreeSurfer toolbox (http://surfer.nmr.mgh.harvard.edu) (Figure 6), These GM ROIs were dilated to spatially coherent brain regions and overlapping regions between WM and dilated GM regions were created as an interface regions between WM and GM. These WM/GM interface masks were used for seed-to-target probabilistic tractograph and later to construct a brain network matrix. Additionally, boundary regions between GM and cerebrospinal fluid (CSF) were extracted for use as a stop mask to reduce artificial brain connections such as tracts jumping across hemispheres through CSF or GM edge. More details on the extracted interface ROIs are shown in Table 3.

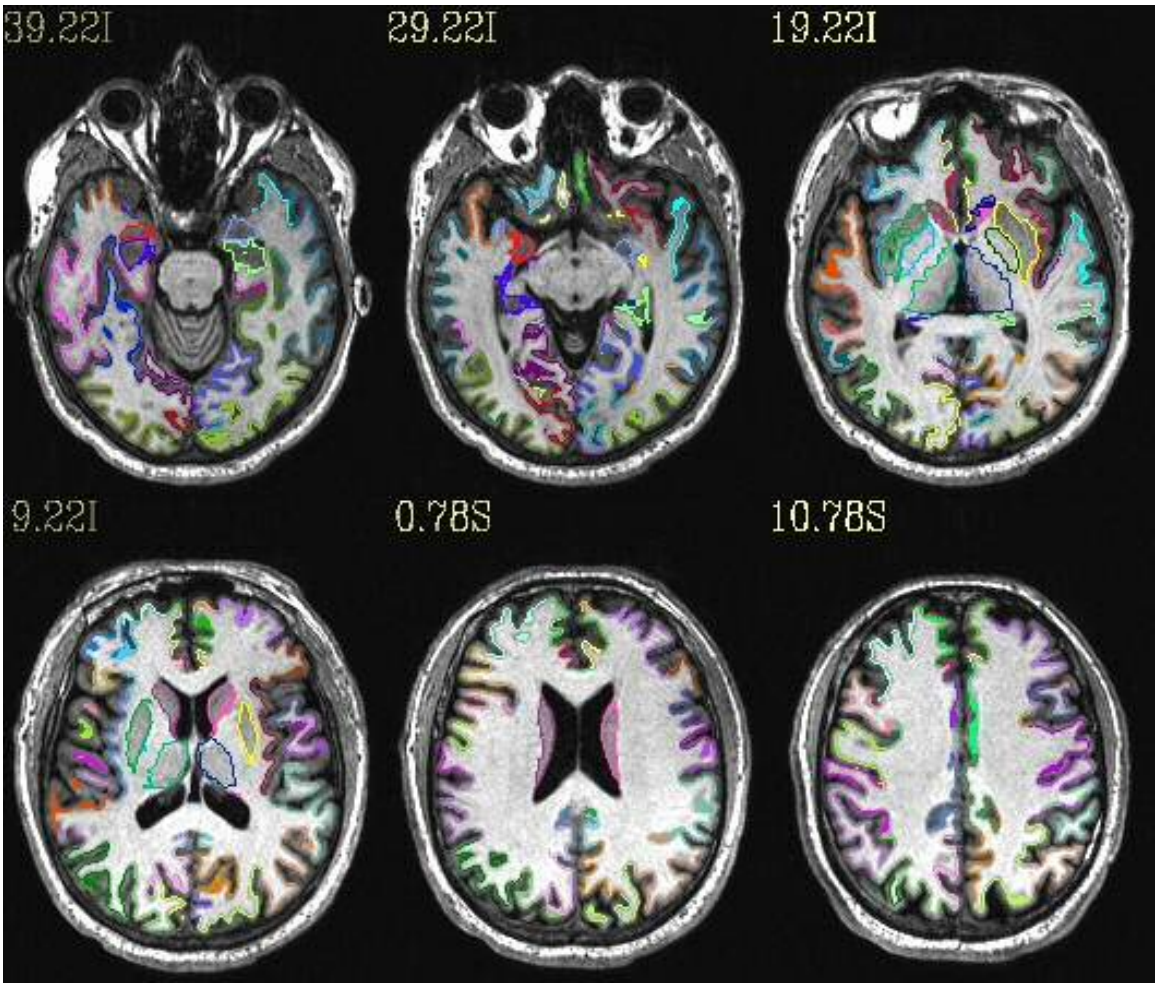

Figure 6. Eighty-four cortical and subcortical WM/GM interface regions of interests for the brain network analysis (see Table 3 for detail region index)

Table 3. Extracted anatomical region of interest labels

(L, R)	Extracted ROI label	(L, R)	Extracted ROI label
(1, 43)	Thalamus	(22, 64)	Middle temporal gyrus
(2, 44)	Caudate	(23, 65)	Parahippocampal gyrus
(3, 45)	Putamen	(24, 66)	Paracentral lobule
(4, 46)	Nucleus Accumbens	(25, 67)	Opercular part of inferior frontal gyrus
(5, 47)	Hippocampus	(26, 68)	Orbital part of inferior frontal gyrus
(6, 48)	Aygdala	(27, 69)	Triangular part of inferior frontal gyrus
(7, 49)	Pallidum	(28, 70)	Pericalcarine
(8, 50)	Bankssts	(29, 71)	Postcentral gyrus
(9, 51)	Caudal (dorsal) part of anterior cingulate gyrus	(30, 72)	Posterior cingulate gyrus
(10, 52)	Posterior part of middle frontal gyrus	(31, 73)	Precentral gyrus
(11, 53)	Corpus Callosum	(32, 74)	Precuneus
(12, 54)	Cuneus	(33, 75)	Rostral part of anterior cingulate gyrus
(13, 55)	Entorhinal area	(34, 76)	Anterior part of middle frontal gyrus
(14, 56)	Fusiform gyrus	(35, 77)	Superior frontal gyrus
(15, 57)	Inferior parietal lobule	(36, 78)	Superior parietal lobule
(16, 58)	Inferior temporal gyrus	(37, 79)	Superior temporal gyrus
(17, 59)	Isthmus of cingulate gyrus	(38, 80)	Supramarginal gyrus
(18, 60)	Lateral occipital gyrus	(39, 81)	Frontal pole
(19, 61)	Lateral orbital gyrus	(40, 82)	Temporal pole
(20, 62)	Lingual gyrus	(41,83)	Transverse temporal gyrus
(21, 63)	Medial orbital gyrus	(42, 84)	Insula

L: Left, R: Right

3.2.4. Construction of structural connectivity network

The procedure for deriving the brain structural connectivity map is shown in Figure 7. To reconstruct the whole-brain WM network and to derive the structural connection map among the aprior-selected 84 interface ROIs, probabilistic tractography (Fdt, http://www.fmrib.ox.ac.uk/fsl) was used. First, probabilistic density functions of primary and secondary diffusion orientation in each voxel were estimated (89). Second, seed-to-target probabilistic tractography was applied from each WM/GM interface mask (seed) to each of the other 83 masks (target) by sampling 1000 streamline fiber per voxel. The number of probabilistic streamlines starting from one ROI (i) to reaching another ROI (j) was counted as the connectivity probability. The connectivity probability from i to j is not necessarily equivalent to the probability from j to i because the probabilistic tractography is dependent on the seed location and their probabilistic density functions. However, these two probabilities are highly correlated across the brain regions (99). Therefore, probability P_{ij} (equivalent P_{ji}), between region i and j, was averaged by these two probabilities to build a symmetric undirected connectivity network matrix.

After the symmetric probability connectivity matrix was derived, it was divided by the mean of the areas (S) of the paired WM/GM interface mask regions, $\frac{S_i+S_j}{2}$, to normalize for the area differences across the brain (98). Finally, an 84 * 84 symmetric matrix was generated and this normalized connectivity matrix was termed the graph of normalized connectivity density (NCD) (106, 117).

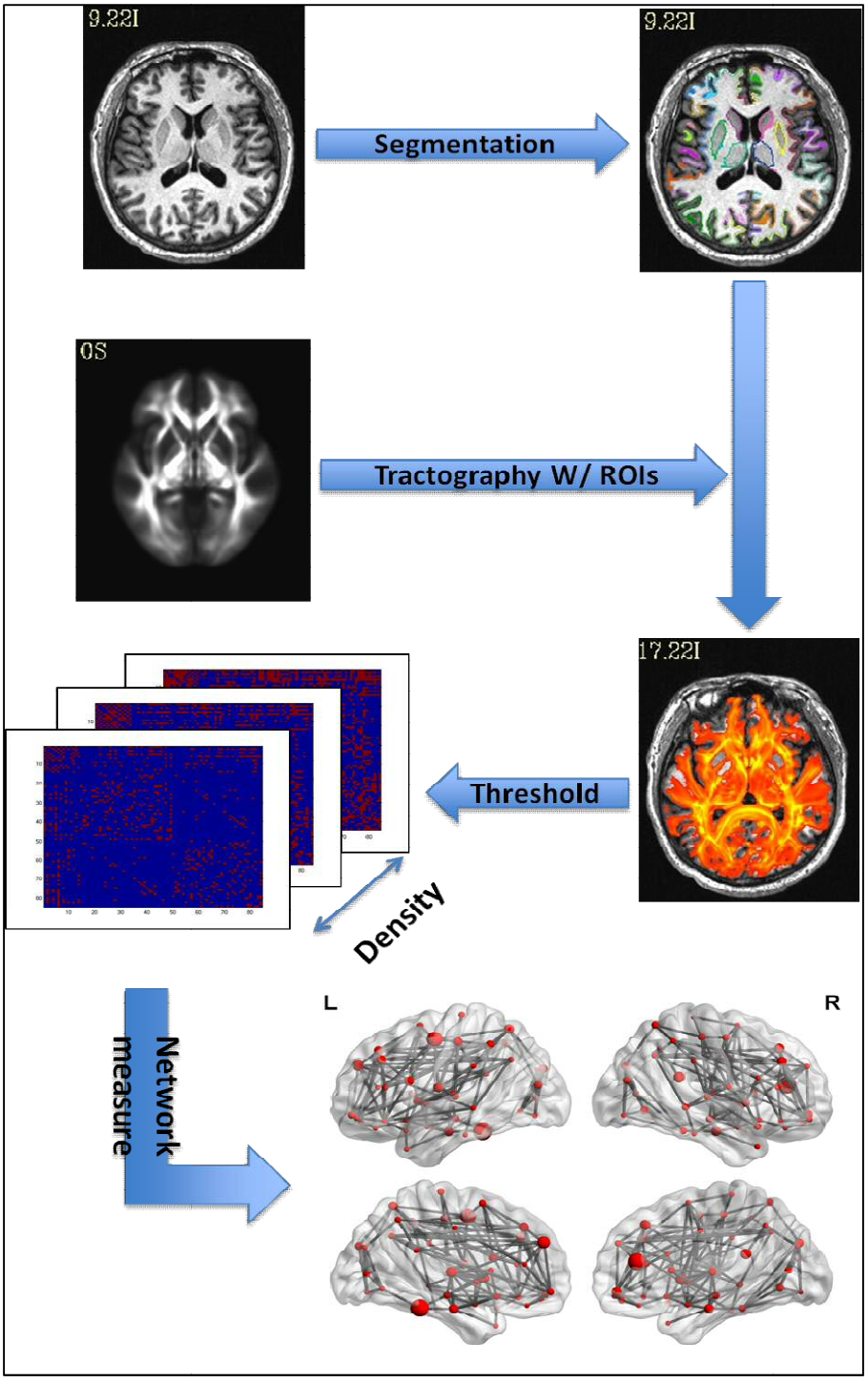

Figure 7. A flowchart for the construction of the WM network by DTI, 1) Parcellate of T1-weighted structural MRI, 2) The reconstruction of all of the WM fibers in the whole brain using probabilistic tractography, 3) The binary networks of each subject were created by threshold along network density, 4) The nodes and connections were mapped onto cortical surface.

3.2.5. Threshold for binary network based on network density

To remove false positive connections, the probability connection was thresholded into a binary matrix with a series of threshold value ranges (98). Network density was used to find the threshold. Network density was defined as the ratio of the number of connections between paired regions over the number of all possible connection in the brain (99, 118). Setting a network density threshold ensures that all the resultant networks have the same number of edges. There is currently no definitive way to determine single threshold value instead of network density with a range of threshold. In the present study, the whole range of network density, 0% to 100%, at an interval of 0.5% was first carefully evaluated. Finally, we used a range of network density, 10% to 30%, at an interval level of 0.1% based on previous study (119) because it allows prominent small-world properties in brain networks to be observed (119). Through this thresholding procedure, a set of undirected and binary network matrixes was obtained for each subject.

3.2.6. Network analysis

For the undirected and binary WM network, both global (small-world properties) and regional network matrices were calculated. The global matrices included: degree (k_i), characteristic path length (L_i), clustering coefficient (C_i), global efficiency (E_{glob}), local efficiency (E_{loc}), and small-worldness (SW). The regional matrices included: nodal degree (k_i) and nodal betweenness centrality (BC_i). Nodes with high degree or high

centrality are defined as a hub and represent important components for efficient communication, providing regulation of information flow (101). All graph-theoretic measures were calculated using the Matlab functions implemented in Brain Connectivity Toolbox (http://www.brain-connectivity-toolbox.net) (104).

3.2.6.1. Random networks

Networks were generated using random processes. In order words, artistry matrix, which has same size matrix as brain network matrix, was randomly generated. These are used as reference networks to confirm the existence of various small-world network properties.

3.2.6.2. Regular networks

Regular networks are ones in which every node has the same number of connections. Similar to random networks, these can be used as reference to verify the existence of small-world network properties in other networks.

3.2.6.3. Network degree

The network degree is the number of links that connect a node. It corresponds to the number of potential inter-regional connections. Network degree is defined as follows (Eq. 1).

$$\mathbf{k_i} = \sum_{\mathbf{j \in N}} \mathbf{a_{ij}} \qquad \textbf{Eq. 1.}$$

Where k_i means the network degree of node i and a_{ij} is the connection between i and j (a_{ij} = 1when link (i,j) exists, otherwise a_{ij} = 0).

3.2.6.4. Characteristic path length

The characteristic path length (CPL) is the mean distance from one node to another. CPL between each pair of regions is commonly expressed according to the estimated physiological properties of the corresponding anatomical connection. The inverse of CPL indicates integrity or closeness centrality of node. CPL is defined as follows (Eq. 2).

$$\mathbf{L = \frac{1}{n}\sum_{i\in N} L_i = \frac{1}{n}\sum_{i\in N} \frac{\sum_{j\in N, j\neq i} d_{ij}}{n-1}} \qquad \textbf{Eq. 2.}$$

Where L_i is the average distance between i and all other nodes, and d_{ij} is shortest path length between node i and j.

3.2.6.5. Clustering Coefficient

The clustering coefficient of a node, i, was defined as the likelihood that the neighborhoods were connected with each other. A relatively high clustering coefficient indicates the presence of tightly knit anatomical groups. The clustering coefficient of a node is defined as follows (Eq. 3).

$$\mathbf{C} = \frac{\mathbf{1}}{\mathbf{n}} \sum_{\mathbf{i} \in \mathbf{N}} \mathbf{C_i} = \frac{\mathbf{1}}{\mathbf{n}} \sum_{\mathbf{i} \in \mathbf{N}} \frac{\mathbf{2t_i}}{\mathbf{k_i(k_i - 1)'}} \quad \textbf{Eq. 3.}$$

Where C_i means the clustering coefficient of node i.

3.2.6.6. Global efficiency

The global efficiency is a measure of how much parallel information can potentially be transferred over the network. It reflects the potential parallel exchange of neural information between involved anatomical regions, e.g., high global efficiency point to highly parallel information transfers in the brain. Global efficiency is defined as follows (Eq. 4).

$$\mathbf{E_{glo}} = \frac{\mathbf{1}}{\mathbf{n}} \sum_{\mathbf{i} \in \mathbf{N}} \frac{\sum_{\mathbf{j} \in \mathbf{N}, \mathbf{j} \neq \mathbf{i}} \mathbf{d_{ij}^{-1}}}{\mathbf{n-1}} \quad \textbf{Eq. 4.}$$

Global efficiency is an inverse of CPL.

3.2.6.7. Local efficiency

The local efficiency reveals how much the network is fault tolerant, showing how efficient the communication is among the first neighbors of node I when node I is removed. It reflects the potential tendency for the existence of communities or clusters of anatomically and physiologically different regions that deal with common neural information. Local efficiency is defined as follows (Eq. 5).

$$E_{loc} = \frac{1}{n}\sum_{i\in N} E_{loc,\,i} = \frac{1}{n}\sum_{i\in N} \frac{\sum_{j,h\in N, j\neq h}(d_{jh}(N_i))^{-1}}{k_i(k_i-1)} \qquad \textbf{Eq. 5.}$$

Where d_{jh} (N_i) is the length of the shortest path between j and h, with only the neighbors of i included.

3.2.6.8. Small-worldness index

The term small-world properties were originally suggested by Watts and Stogatz (120) and it refers to the concept that the brain is organized as small-world structure, which has a highly efficient neuronal architecture (121). The small-world structure means that the brain has significantly more clustered than random networks and has similar characteristic path length as a random network. In physiological interpretation, small-world networks have higher local efficiency than random networks and higher global efficiency than regular networks (networks in which every node has the same number of connections) (122). Small-worldness is defined as follows (Eq. 6).

$$SW = \frac{C/C_{rand}}{L/L_{rand}} \qquad \textbf{Eq. 6.}$$

Where C is the clustering coefficient and L is the characteristic path length. Rand is the random network. Small-world networks (SW) often have SW >> 1. To examine the small-world properties of participants, the following three steps analysis was investigated;

1) the clustering coefficient and characteristic path length of participant networks were compared with random networks, 2) small-worldness (SW) was evaluated compared to network density, 3) local and global efficiency of participant networks were compared with random networks and regular networks, respectively.

3.2.6.9. Nodal betweenness centrality

The nodal betweenness centrality (BC) is a widely used quantity and can be used to express the structural importance of these nodes. It is denoted as the fraction of shortest paths between pairs of nodes that pass through a given node. Specifically, the BC of a weighted network is given as follows (Eq. 7).

$$\mathbf{BC_i^w} = \sum_{\mathbf{k,j \in G_{k \neq j \neq i}}} \frac{\boldsymbol{\sigma_{kj}^w(i)}}{\boldsymbol{\sigma_{kj}^w}} \qquad \textbf{Eq. 7.}$$

Where G is the graph, σ_{kj}^{w} is the number of all shortest paths from node k to node j, and $\sigma_{kj}^{w}(i)$ is the number of shortest paths passing through node I in a weighted graph.

3.2.6.10. Area under curve for each network measures

To provide a summarized scalar for topological characterization of brain networks independents of single threshold, the area under the curve for each network metric was calculated. The integrated AUC metric is sensitive to detecting topological abnormalities in brain disorders (114, 123-125).

3.2.7. Statistical analysis

To test for group differences in age, gender, and duration of illness, the data was analyzed using a t-test or χ^2 test. These are provided in Table 2 (Chapter 2). To determine statistically significant group differences in network measures, nonparametric permutation tests (90) were performed on the AUC of each network measure. For the network centrality analysis, t-tests were performed between the MDD and control groups for both degree and betweenness centrality.

3.3. Results

3.3.1. Small-world structural network

The topological properties of brain networks depend on the choice of threshold. In this study, we first examined small-worldness properties, including clustering coefficient, characteristic path length, global-/local-efficiently, and measures of network small-worldness index (SW), at a range of 0% to 100% to find a definitive range of threshold value that show small-world characteristics. Mean SW index of all participants was greater than 1 through the entire range of network density (Figure 8), which is a typical feature of a small-world network. Moreover, structural brain networks of both MDD and control groups had higher clustering coefficient and identical characteristic path length

when compared with matched random networks (Figure 9). These results suggest that structural brain networks of both MDD and control groups have small-world architecture.

Furthermore, all brain networks along the entire network density range demonstrated an economic small-world topology as follows; 1) higher global efficiency of networks in both MDD and control groups compared to random networks, 2) approximately equivalent parallel information processing of global efficiency but a higher fault tolerance of local efficiency compared to random networks, 3) both global and local efficiency rose much faster than the required wiring cost (network density) (e.g., approximately 15% network density, the structural brain networks reached 50% of local and global efficiency) (Figure 10 & 11).

In this study, range of network density from 10% to 30% was used because the network density of mammalian brain network is estimated to be higher than 10% (98, 119, 126, 127) and 30% network density was previously demonstrated in various studies (117, 128).

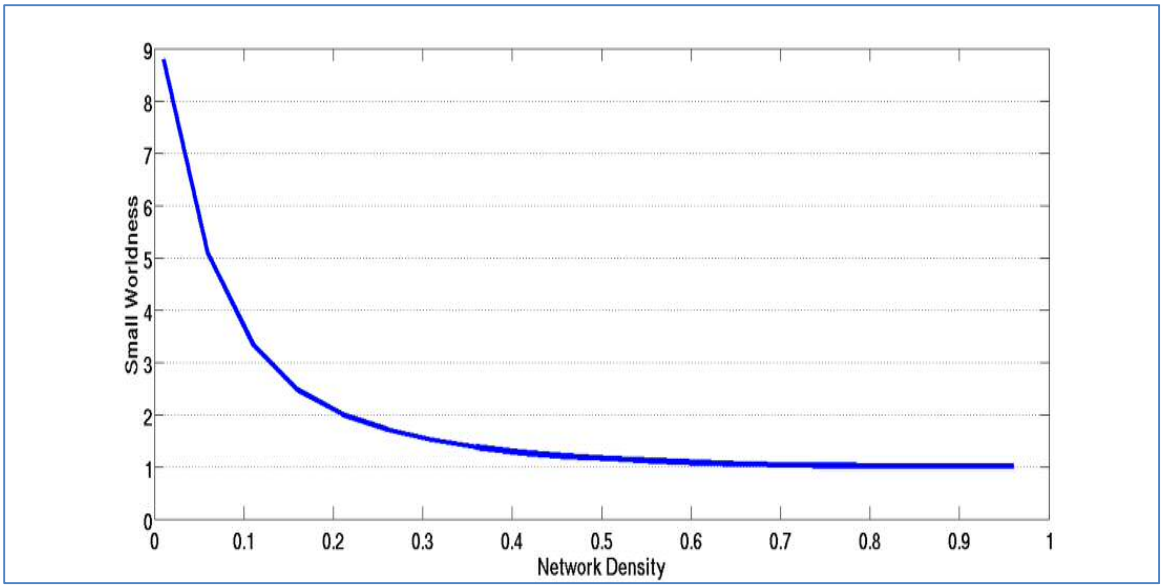

Figure 8. Mean small-worldness index of all participants as a function of network density (cost). Small-world networks often have S >> 1 and it suggests that structural brain networks show small-world properties.

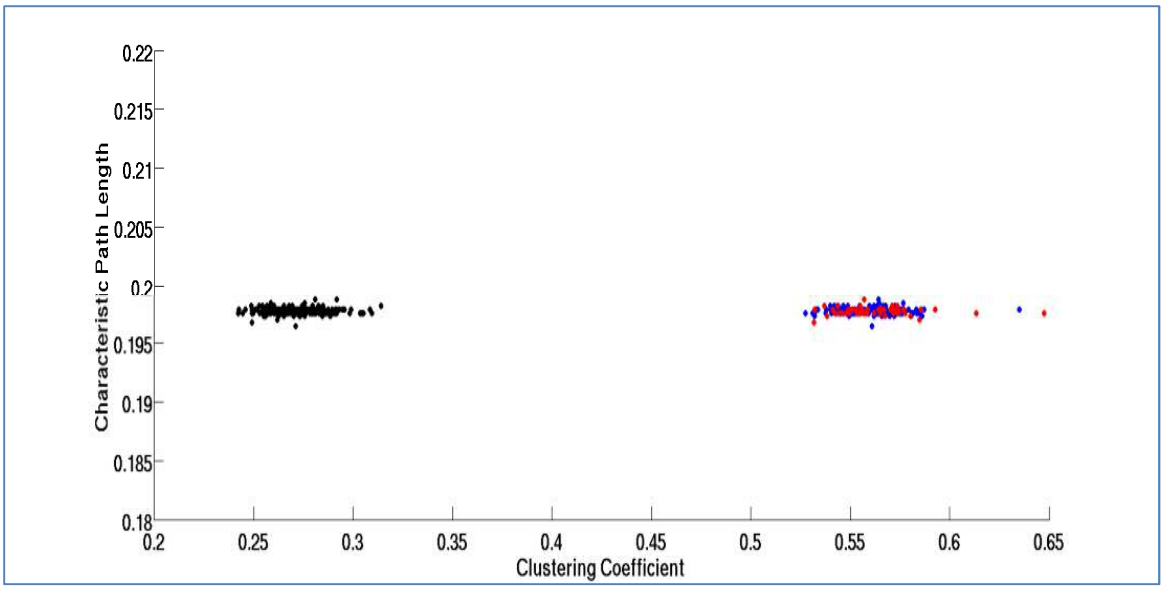

Figure 9. Small-world properties (clustering coefficient and characteristic path length) of structural brain networks. Red: MDD group, Blue: control group, Black: random network matched to all participants. Structural brain networks of both MDD and control group show higher cluster coefficient and equal characteristic path length compared with random networks. It is typical feature of small-world network.

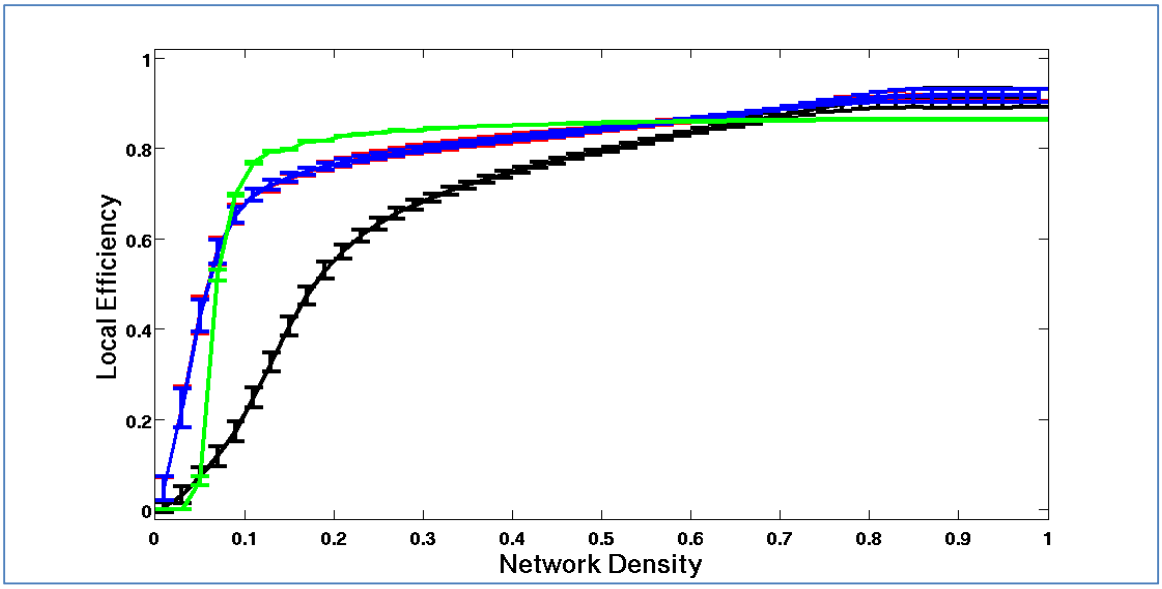

Figure 10. The local efficiency of random (Black), regular (Green) and structural WM brain networks (Red & Blue) as a function of network density. The brain networks under 5% ~ 60% network density showed higher local efficiency than matched random networks.

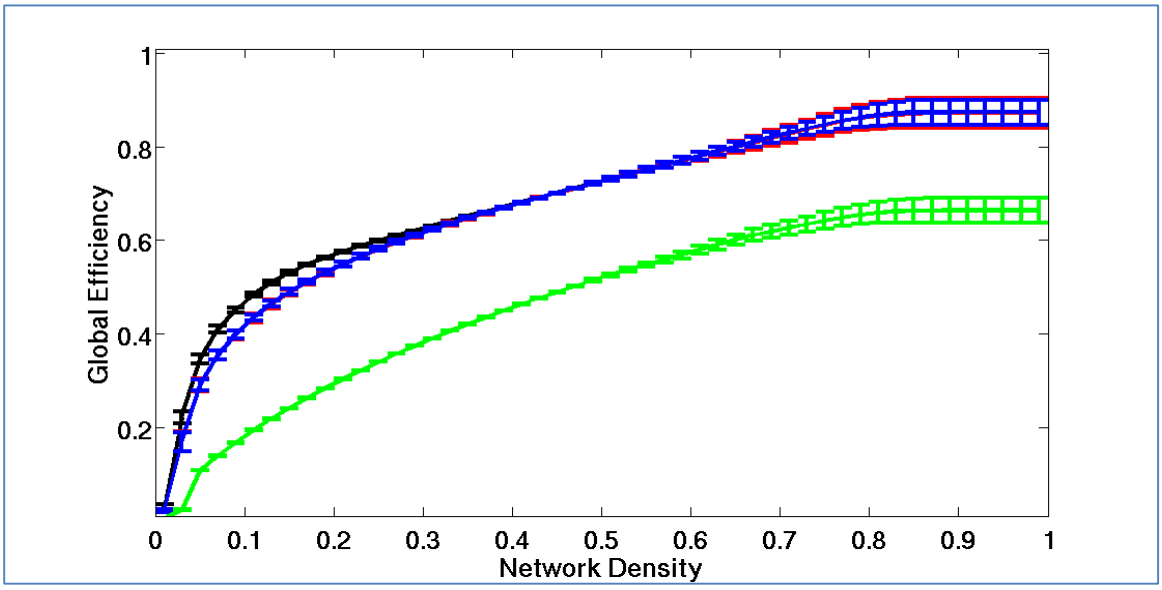

Figure 11. The global efficiency of random (Black), regular (Green) and structural WM brain networks (Red & Blue) as a function of network density. The brain networks under each network density value showed higher global efficiency than matched regular networks.

3.3.2. Alteration of global characteristics in MDD

Non-parametric statistical analysis revealed no significant differences between MDD and control groups in global network measures including degree (k_i), characteristic path length (L_i), clustering coefficient (C_i), global efficiency (E_{glob}), and local efficiency (E_{loc}). It indicates that both MDD and control groups have identical network's capacity to transfer information globally. In other words, MDD group does not show abnormal global disruption of network's capacity.

3.3.3. Alteration of regional nodal characteristics in MDD

Compared with the healthy control group, the MDD group showed decreased nodal centrality in left caudate, left middle cingulate cortex, left and right inferior parietal lobule, right anterior cingulate cortex, and dorsal lateral prefrontal cortex. It indicates the structural connections from- and to- these regions are depicted and it associated to MDD. The MDD group showed increased nodal centrality in left superior temporal gyrus and right inferior frontal gyrus (Table 4 and Figure 12) compared with the healthy control group

Table 4. Brain regions showing abnormal nodal centrality in MDD compared with healthy control group

	p-value	
MDD > Control	**Degree**	**BC**
Left Superior temporal gyrus	**0.0052**	**0.0032**
Right Inferior frontal gyrus (orbital part)	**0.0053**	0.1682
MDD < Control		
Left Caudate	**0.0191**	**0.0157**
Left Anterior cingulate gyrus (caudal part): dACC	**0.046**	**0.0298**
Left Inferior parietal lobule	0.1833	**0.0072**
Right Inferior parietal lobule	**0.0416**	0.088
Right Anterior cingulate gyrus (rostal part): rACC	0.0516	**0.0267**
Right Middle frontal gyrus (anterior part): DLPF	**0.0023**	**0.00001**

MCC: middle cingulate cortex, ACC: Anterior cingulate cortex, DLPF: dorsal lateral prefrontal cortex

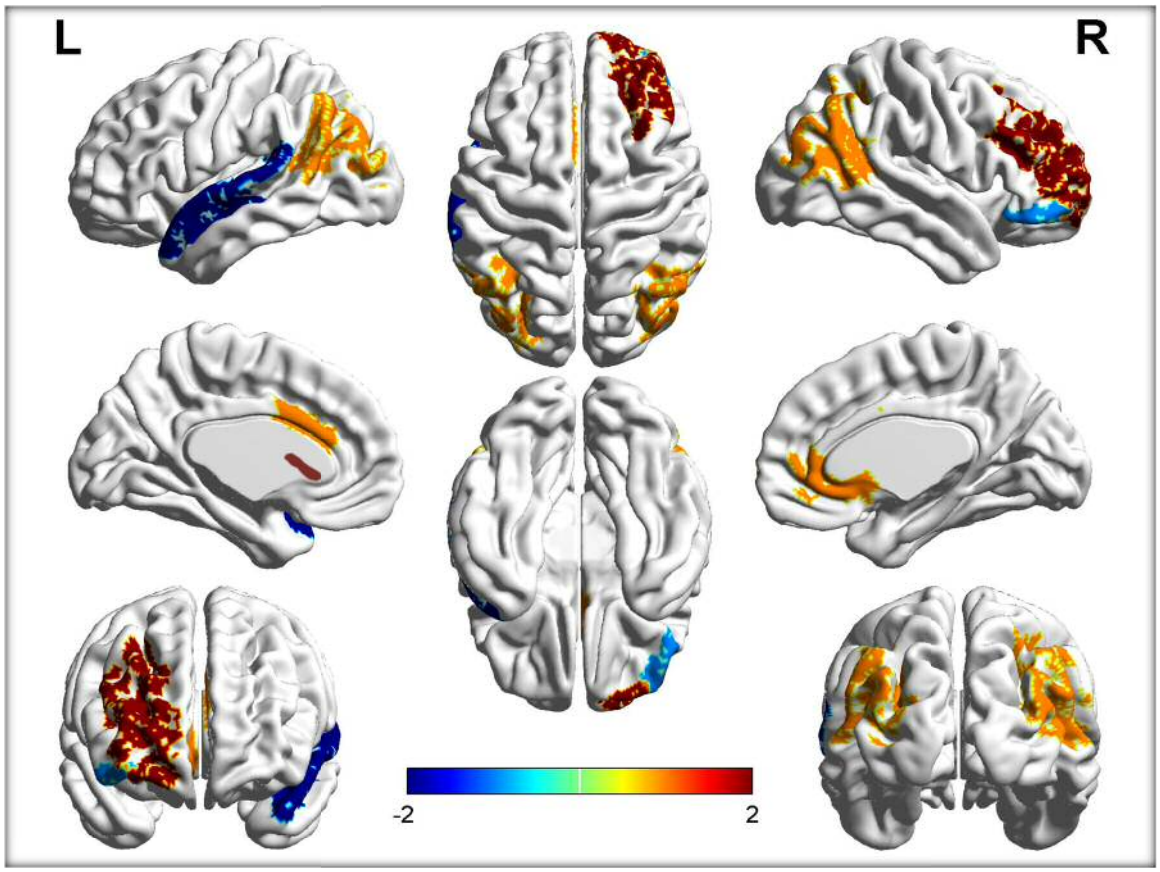

Figure 12. Brain regions showing abnormal nodal centrality in brain structural networks (See table 4 for detail). Red: MDD < Control, Blue: MDD > Control, intensity: one or two centrality measure overlapped.

3.4. Discussions and Conclusion

This is the first study to use graph analyses of probabilistic tractography to compare the topological organization of structural brain networks between MDD patients and healthy controls. Although the results of the global integration did not show statistical significance between MDD and control groups, network centrality analysis suggests that many local brain regions were affected by MDD: decreased nodal centrality were seen in left caudate, left dorsal anterior cingulate cortex, left and right inferior parietal lobule, right rostal anterior cingulate cortex, and dorsal lateral prefrontal cortex, while increased nodal centrality was seen in left superior temporal gyrus and right inferior frontal gyrus. These results provide insights into our understanding of altered topological organization in structural brain networks of MDD.

Small-world concept provides an attractive model for characterizing brain networks because it supports two fundamental organizational principles in the brain: integration and segregation(129). Networks that are cheap to build but still efficient in propagating information are said to be economic small-world networks. Here, we found that MDD patients and healthy controls showed both conventional and economic small-world properties of the WM networks, characterized by high local clustering and short path length, which are in accordance with previous WM network studies in healthy adults (98, 99). Moreover, it shows high efficiency at low wiring cost (67).

We used regional network centrality measures, including betweenness and degree, to find localized network differences between MDD and control group. Nodes with high structural degree and betweenness centrality suggest regions that are highly interactive and that have the potential to participate in a large number of functional integrations. A novel finding of this study was the identification of a decreased tendency of nodal centrality in caudate, anterior cingulate cortex, dorsal anterior cingulate cortex, inferior parietal lobule, and dorsal lateral prefrontal cortex. These findings are consistent with functional imaging studies that suggested dysfunctions in these regions in the pathophysiology of depression (50, 130-139).

Both the rostal and dorsal anterior cingulate have been implicated in the regulation of emotions and cognition (130-133). Many neuroimaging studies of MDD demonstrate functional abnormalities in ACC (133, 134), and in the relationship between metabolic activity of ACC and treatment response (decreased activity in subgenual ACC regions (50) but increased activity in dorsal ACC (dACC) regions (135) associated with successful antidepressant treatment). Recent fronto-cingulate studies also demonstrate abnormal functional connectivity among the rACC, dACC, and DLPF (133). For example, studies report reduced functional connectivity from the DLPF to the rACC (136, 137) and to the dACC (138, 139) in MDD during cognitive and/or affective challenges. This deficiency of functional connectivity might be related by this lower structural interaction (connection) between these regions.

The caudate nucleus, a basal ganglia structure, is known to be involved in the control of motor, cognitive, and emotional processes. Previous functional studies report reduced functional activity in the caudate (140) and reduced functional connectivity of the caudate to the default mode network (DMN) (141) are associated with depression. In addition to functional studies, structural investigations report reduced gray matter volume (142) in caudate associated with depression. The convergence of these data with our results suggests an important role of caudate structural connectivity in the pathophysiology of depression.

Although the inferior parietal cortex (IPC) is a functionally heterogeneous region and its contribution to complex brain functions is poorly understood, a recent study using an emotional audiovisual task suggests aberrant neural response in audiovisual processing in depression. (143). These abnormalities in structural connectivity of the IPC region in our study further validate a role for this region in the biology of MDD.

While there are no statistical differences between MDD patients and healthy control subjects in global topological brain organization, there are differences in network derived nodal centralities, specifically degree and betweenness centrality. These results increase our understanding of the neural basis of MDD by demonstrating aberrant network organization in specific regions in MDD patients. The deficiencies of regional connectivity in MDD coincide with previously described roles for fronto-cingulate circuit and IPC in the neurobiology in this disorder. These findings have implications for understanding how the topological alterations in large-scale brain networks underlie

structural deficits in major depressive disorder. The topological network analysis also provides a new way to understand the neurobiology of specific structural deficits that can't elucidate by voxel-wise white matter integrity analysis.

CHAPTER 4

Defining critical WM Pathways Mediating Successful Subcallosal Cingulate Deep Brain Stimulation for Treatment-Resistant Depression

As described in previous chapters, it have been clarified that disrupted WM integrity does not play a major role in the neurobiology of MDD (Chapter 2). Moreover, network analysis with tractography and graph theory provides a powerful method for quantifying the topological organization of WM connection differences between MDD and control groups. It allows detecting WM connection deficit in MDD (Chapter 3).

In the past decade of search for better treatments for depression, increasing interest has focused on focal neuro-modulation. This focus has been driven by improved neuro-anatomical models of mood, thought, and behavior regulation, as well as by more advanced strategies for directly and focally altering neural activity. Deep brain stimulation (DBS) is one of the most invasive focal neuro-modulation techniques available; data have supported its safety and efficacy of treatment (31, 58, 144-146). DBS is achieved by implanting one or more electrode arrays (leads) into a specific region of the brain via burr holes in the skull using neuroimaging guided stereotactic neurosurgical techniques. Currently, electrode placement is based on local SCC anatomy with clinical efficacy assessed using standardized symptom severity scales. Clinical response may be improved by more precise targeting along specific white matter tracts based on network connection pattern. Structural connectivity pattern analyses using diffusion tractography

may help us address the clinical effectiveness of DBS by indentifying the necessary and efficient network pattern in responders. In this chapter, extending of WM network analysis to clinical application in depression, primary impact WM pathways that is mediating antidepressant response for SCC WM DBS was identified and assessed using diffusion tractography.

4.1. Introduction

For patients with treatment-resistant depression (TRD), deep brain stimulation (DBS) is an emerging experimental therapy. In the past decade, a number of different stimulation sites have been investigated including the subcallosal cingulate white matter, the ventral capsule/ventral striatum, the nucleus accumbens, the lateral habenula, the inferior thalamic peduncle and the medial forebrain bundle (12, 78, 147-150). Six month response rates across studies range from 41%-66% with sustained or increased response over time. Of the various DBS targets for treating TRD, SCC white matter has been the most studied with published data available for 71 patients implanted at seven separate centers. Within some cohorts, outcome data for patients receiving more than six years of chronic SCC DBS suggest significant and lasting antidepressant efficacy. An industry sponsored clinical trial is now in progress (15, 77, 151-155).

Targeting the SCC white matter was based on converging imaging data demonstrating changes in SCC activity with antidepressant response to a variety of

standard treatments (31, 58, 144-146). Selection of this target was further supported by an extensive literature demonstrating monosynaptic connections between the subcallosal cingulate and specific frontal, limbic, subcortical and brain stem sites involved in mood regulation, depression and the antidepressant response (35, 156-161). Specific placement of the DBS electrodes was therefore driven by local anatomy: approximate coordinates were derived from previous PET imaging studies localizing the subcallosal cingulate region (Brodmann Area 25) and adjacent white matter, combined with anatomical landmarks identified in standard neurosurgical atlases (Figure 13) (162).

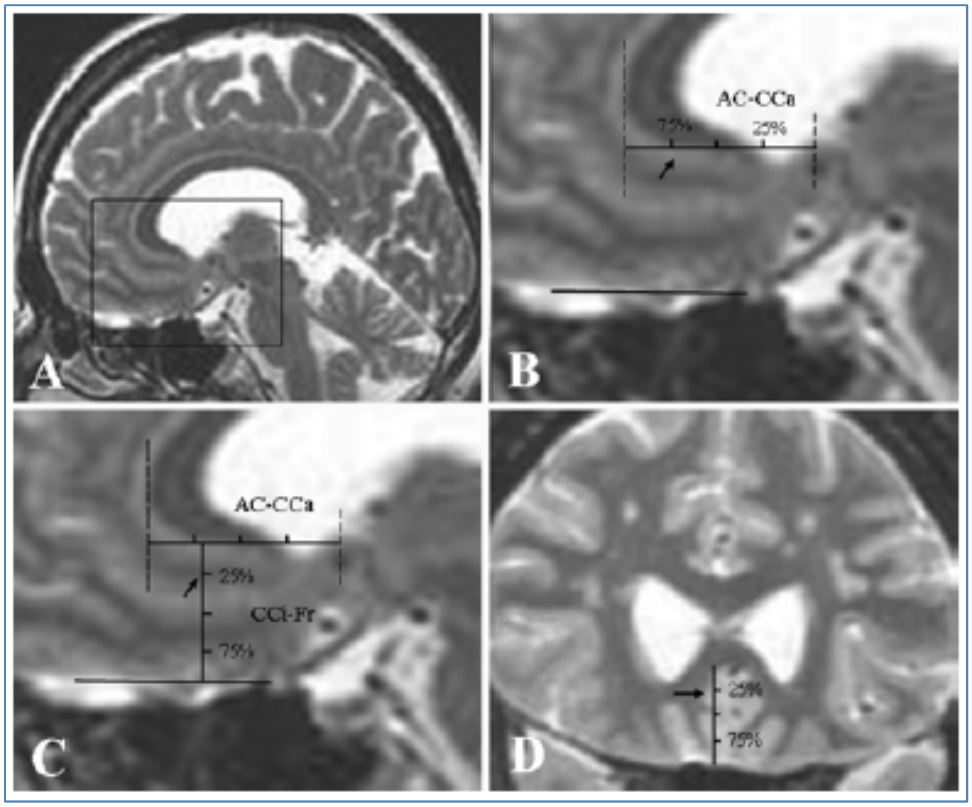

Figure 13. Anatomical location based the standardized method for targeting the SCG. A: Sagittal section showing the SCG. (Panels B and C are magnified images that correspond to the square in A.) B and C: To target the SCG, a line is initially traced parallel to the base of the Fr. Thereafter, AC-CCa and CCi-Fr lines are to be drawn parallel and perpendicular to the base of the frontal lobe, respectively, and divided into quartiles. D: Axial and/or coronal planes of a region corresponding to 70–75% in AC-CCa and 25–30% in CCi-Fr should then be selected to define the anatomical gray/white matter junction of the SCG. SCG: subcallosal cingulate gyrus, AC: anterior commissure, CC: corpus callosum, CCa: anterior aspect of the CC, CCi: inferior portion of the CC, Fr: Frontal lobe (Hamani, Mayberg et al. (163)).

Although SCC DBS is associated with notable antidepressant effects in patients with TRD, the magnitude of the response varies. First steps to define responder and non-responder differences focused on the anatomical location of the active contacts used for

chronic stimulation indexed using standardized anatomical metrics performed on post-op 1.5T structural T1 MRI images, but these studies found no differences among response subgroups (163). Comparable anatomical targeting in responders and non-responders was confirmed in a second cohort of patients using comparable localization methods (151).

Additional studies further suggested that activity changes in areas remote from the stimulation target, such as the dorsal cingulate and frontal cortex, were potentially most important to a full antidepressant response versus local activity changes around the SCC DBS target (12). However, small sample size precluded definitive, clinically meaningful conclusions based on these observations.

Paralleling these ongoing clinical DBS studies, functional and structural neuroimaging methods have advanced rapidly (13, 67, 97, 164, 165), providing new strategies to examine responder-non-responder differences with an eye towards optimizing the surgical procedure and improving clinical outcomes. Studies of DBS mechanisms have similarly progressed with a shift in focus from local changes in cell bodies at the stimulation site to a more complex combination of local and remote effects (166-169). Axonal elements directly modulated by DBS (afferents and efferents projecting to and from the SCC, as well as fibers of passage) may be especially important to the antidepressant effects of the stimulation (170-177). Delineation of the various impacted white matter pathways is a next step to optimize the clinical procedure as well as better characterize the putative mechanisms of action.

Diffusion tensor imaging (DTI), by quantifying the local diffusivity of water molecules in the brain tissue, allows delineation of direction, orientation and integrity of the white matter. Then, white matter connections between different brain regions can be calculated using tractography algorithms (89, 178-185).

Using fiber tractography approaches (89), the connections of the SCC have been previously mapped in healthy subjects, confirming the midline frontal, cingulate, medial temporal, striatal, thalamic, hypothalamic and brainstem pathways previously characterized in non-human primates and implicated through PET studies of blood flow change with chronic stimulation (13, 14, 157, 186, 187).

In applying tractography to the study of white matter connections of a specific DBS target, it is important to understand that DBS generates an electric field that is applied to the various neural elements surrounding the electrode. The response of those neural elements is dependent upon the electrode location and stimulation parameter settings, which are specific to each patient. Detailed computational models of the DBS activation volume have previously been developed (Figure 14) (174, 188) and successfully applied to the study of DBS in Parkinson's disease (189). Therefore, a goal of this study was to adapt the concepts of DBS activation volumes to the study of the SCC target.

To define the necessary and sufficient tracts for antidepressant response from SCC DBS we modeled individual probabilistic tract maps in patients enrolled in a clinical

trial of SCC DBS for TRD. We hypothesized that specific tract maps from the active DBS contact would be associated with clinical response after six months of chronic SCC DBS.

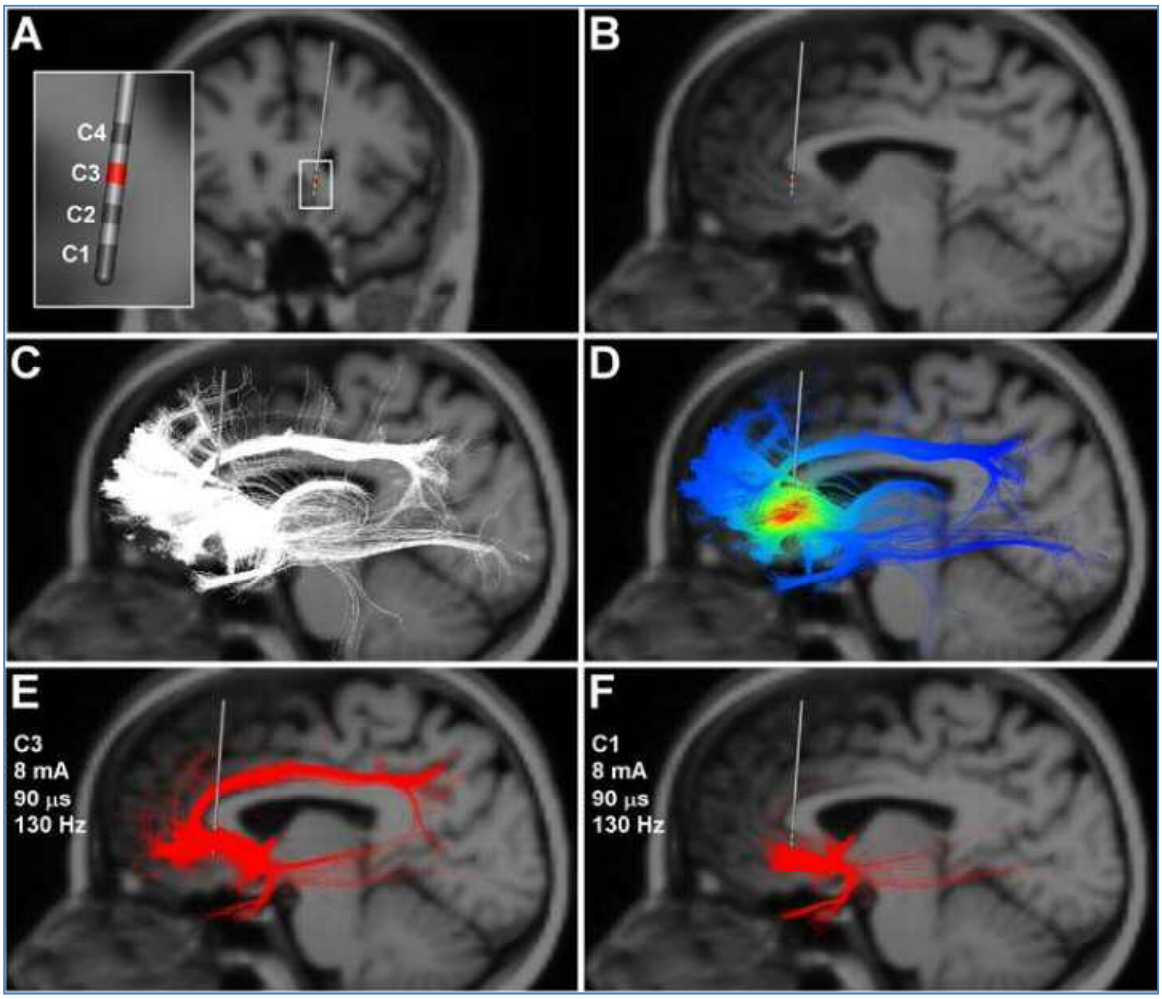

Figure 14. Demonstration of small anatomical location change cause different tract connections. A) Coronal image of the DBS electrode location. Inset shows the St Jude four contact electrodes and the respective contact numbers. Stimulation through contact 3 resulted in the best clinical outcomes. B) Sagittal view of the DBS electrode location. Note that the MRI background image is 3 mm behind the tip of the DBS electrode as not to obscure the tractography results which project in 3D around the electrode. C) White streamlines represent axon model trajectories passing by the DBS electrode. D) Voltage distribution imposed upon each axon model from stimulation at contact 3. E) Axon models (red streamlines) directly activated by therapeutic stimulation. F) Axon models directly activated by non-therapeutic stimulation. (Lujan, Choi, Mayberg et al. (190))

4.2. Materials and Methods

4.2.1. Participants and clinical protocol

Seventeen chronically depressed, treatment-resistant patients gave written consent to participate in a research protocol at Emory University testing safety and efficacy of SCC DBS in treatment-resistant depression (15) (clinicaltrials.gov NCT00367003). The protocol was approved by Emory University Institutional Review Board and the US Food and Drug Administration under an Investigational Device Exemption (G060028 held by H.S.M.) and was monitored by the Emory University Department and Behavioral Sciences Data and Safety Monitoring Board.

Patients underwent implantation of bilateral electrodes in the SCC area as previously described (15). Briefly, after a 4-week, single-blind, sham stimulation phase, a 24-week open-label active stimulation phase was conducted. Response was defined here as in the original report of the clinical trial: 50% decrease in HDRS-17 (191). After 6 months of chronic simulation there were 7 responders and 10 non-responders (41%). One of the responders was excluded from analysis due to inadequate quality of the pre-surgical DTI data. The imaging analysis in the responder group was done on 6 patients and on 10 in the non-responders. There were no significant differences in demographics or clinical characteristics between responders and non-responders (Table 5).

Table 5. Demographic and Clinical Characteristics

	Responder N=6	Non-Responder N=10	Statistics Z or $\chi 2$	p
Gender (Female/Male)	3/3	6/4	0.15	0.69
Age, mean (S.D.)	43(12.71)	41.1(7.02)	0.32	0.74
Marital status (single/married/divorced)	3 / 2 / 1	6 / 3 / 1	-	
Years of Education, mean (S.D.)	16.33 (3.27)	16.50 (3.06)	0.22	0.82
Months of current episode, mean (S.D.)	55.66 (44.23)	74.00 (60.28)	0.10	0.91
Age when first depressed, mean (S.D.)	24.33 (10.19)	17.30 (5.38)	1.31	0.18
Lifetime number of depressive episodes, mean (S.D.)	3.83 (3.06)	8.40 (11.56)	0.82	0.40
Lifetime number of hospitalizations, mean (S.D.)	4.66 (3.56)	5.60 (6.77)	0.27	0.78
Lifetime number of suicide attempts, mean (S.D.)	3.33 (4.72)	0.80 (1.03)	1.08	0.27
Lifetime number of antidepressant treatments, mean (S.D.)	19.33 (9.95)	25.7 (10.39)	1.30	0.19

S.D.: Standard Deviation, MDD: Major Depressive Disorder, BP: Bipolar Disorder, Statistics: Z (Mann-Whitney U test), $\chi 2$ (Chi-Square test)

4.2.2. Magnetic resonance and computer tomography imaging

Multi-sequence structural and diffusion MRI was acquired in a single session one week prior to surgery. T1-weighted and DTI data were acquired on a 3T Tim Trio MRI scanner with a 12-channel head array coil (Siemens Medical Solutions, Malvern, PA, USA) that permits maximum gradient amplitudes of 40mT/m. Single-shot spin-echo echo-planar imaging (EPI) sequence was used for DTI with generalized auto-calibrating parallel acquisition (GRAPPA) with two-fold acceleration (R=2) (85). DTI parameters were: FOV = 256 x 256; b value = 1000 sec/mm^2; voxel resolution = 2×2×2 mm; number of slices = 64; matrix = 128 x 128; 2 averaged; 64 non-collinear directions with one non-diffusion weighted images (b=0); TR/TE = 11300/90ms. High-resolution T_1 weighted images were collected using a 3D magnetization-prepared rapid gradient-echo (MPRAGE) sequence with the following parameters: TR/TI/TE = 2600/900/3.02 ms; a flip angel of 8º, voxel resolution = 1×1×1 mm; number of slices = 176; matrix = 224×256.

Post-surgical high resolution CT data were acquired on a LightSpeed16 (GE Medical System) with resolution 0.46×0.46×0.65 mm^3. These data were used to identify the location of DBS contacts which in turn were used to generate the volume of activated tissue (VAT).

4.2.3. DBS Activation Volumes

The DBS contact locations were first identified in native CT space and then transformed to MNI152 space using each individual subject's T_1 MRI space (see below). The patient-specific DBS activation volumes were then defined within the context of MNI152 space. Figure 15 presents an example of the four contacts visible on one subject's T_1 image in CT space. There are 4 individual contacts on each DBS lead. Each contact is 1.4 mm in diameter. The contact at the tip of the array is longer than the other 3 (3 mm vs 1.5 mm, respectively), with each separated by a 1.5 mm non-conductive gap (Libra system, St Jude Medical, Plano, TX). (Figure 15)

Calculation of the DBS activation volumes required some special considerations given the St Jude DBS system and the grey/white matter transitions of the SCC region. Therefore, custom activation volumes were created for this study. The detailed methodology for DBS activation volume prediction is described in Chaturvedi et al. (192), which rely on artificial neural networks (ANNs) to characterize the spatial extent of directly activated axons as a function of the stimulation parameter settings. These ANNs are trained on the results of thousands of simulations that directly couple DBS electric field models with multi-compartment cable models of axons. In addition, the ANNs used in this study have several unique features: 1) explicit representation of the St Jude DBS electrode design, 2) use of current-controlled stimulation, and 3) separate ANNs for representing DBS in grey matter or white matter. Grey matter was represented in the DBS electric field model as an isotropic bulk tissue domain, while white matter

was represented as an anisotropic bulk tissue domain with the axon models oriented parallel to the orientation of high electrical conductivity. (Figure 15)

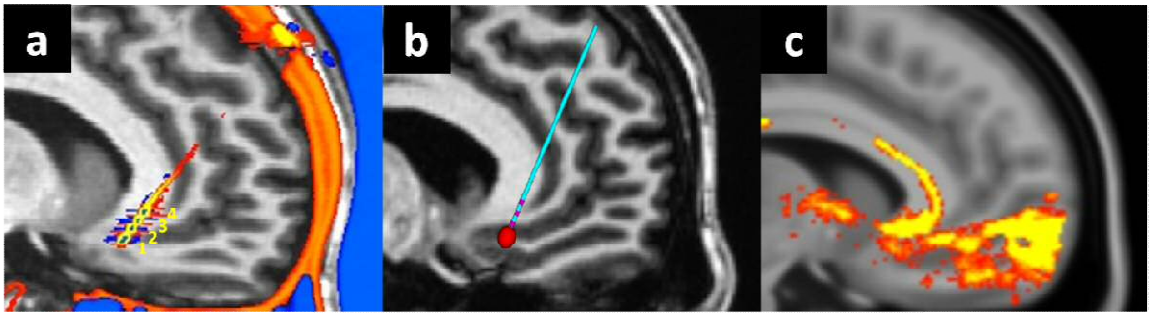

Figure 15. Identification of contact location, a: post-surgical CT image overlapped onto pre-surgical T1 image for one subject. Contacts are numbered inferior to superior, 1 to 4. b: Activation volume using contact 1 and typical parameters for a sample subject (130Hz, 90us, 6mA), c: Probabilistic tractography connection from calculated activated volume for one subject.

4.2.4. Tract Map Generation using Individual VAT seeds

Tract map were generated by following analysis processing.

4.2.4.1. Preprocessing

High-resolution T_1 weighted images were parcellated into cortical and subcortical regions using Freesurfer (http://surfer.nmr.mgh.harvard.edu) for use as a seed-to-target tractography mask and as a stop mask to reduce artificial connections such as crossing hemispheres through cerebrospinal fluid (CSF) or gray matter (GM) edge regions.

Tools within the FSL (http://www.fmrib.ox.ac.uk/fsl, Flirt and Fnirt, Oxford, UK) were used for all image registration and tractography processing (86, 193). First, T_1 and DTI data were skull stripped to remove non-brain regions. Diffusion data underwent eddy current correction, and local DTI fitting (88, 89). CT and diffusion images were co-registered to T_1 image by affine transformation and then normalized to MNI152 template by applying nonlinear transformation information previously calculated by fnirt (FSL) in the nonlinear registration from T_1 to the MNI152 template.

4.2.4.2. Probabilistic Tractography

Probabilistic tractography was performed using Fdt, a diffusion toolbox in FSL (89, 194). Three analyses were performed (a) from VATs to whole-brain; (b) from VATs to regions of interest (seed-to-target) encompassing an expansion of regions identified in the whole-brain analysis; and (c) correlation between connectivity of identified regions and index of response to treatment.

(a) Whole-brain tractography analysis

With the goal to define tracts that are common to all responders, tract maps for each patient were generated using the combined VATs calculated for their two active DBS contacts, one in each hemisphere.

The contacts that were selected for the analysis were the ones that were delivering the stimulation at the 6-month visit. Participants may have changed stimulation contacts before, but the ones that were efficacious in generating

antidepressant response were maintained. Five thousand random samples per voxel were sent out from each individual's bilateral VATs to whole brain. The whole brain fiber probabilistic tractography map was divided by total number of streamline sent out to compensate seed (VAT) size difference, and was then binarized (0.001% was used in the present results, but a series of other thresholds were also tested) (128). Each binary map was added to create the common population map of the structural connections in each group (e.g., all subjects share all voxels). To validate that these common tracts were not biased by specific subjects, a second map defined by shared pathways by 50% of the subjects was generated for comparison.

(b) Seed-to-target tractography analysis

A second analysis was done to elucidate what is different in each individual responder and non-responder. Six cortical and subcortical target regions were selected from WM common pathways of responders, from the whole-brain analysis. These target regions were generated based on combination of the Freesurfer parcellated brain atlas (Desikan-Kiliany atlas) (68, 195, 196) and Harvard-Oxford structural atlas (FSL) (197-199). Three regions in each hemisphere were selected: (1) medial- and orbito-frontal cortex (BA10/BA11), (2) anterior cingulate cortex, and (3) a basal ganglia-thalamic cluster including nucleus accumbens, caudate, putamen, and thalamus. Gray and white matter interface regions were extracted from each of the cortical-subcortical target regions to improve tractography quality (Figure

16, showing targets). Structural connectivity was calculated from paired two brain regions, which are bilateral VATs (N_u) and each brain target region (N_v). For each pair of brain regions, five thousands random samples per voxel were sent from bilateral VATs seed mask, and the total number of probabilistic streamlines started from seed regions and reached the GM/WM interface target region in that pair were summed and counted. After total number of connected streamline was counted for each brain region pair, it was divided by the mean of the areas of the two regions (Eq. 8), where S_u and S_v represent the areas of the bilateral VAT and each brain target mask region to compensate size differences across brain regions, and ($C_{(u,v)}$) is termed the normalized connection (density) (98, 99, 124, 128).

$$C(u,v) = \frac{2(Nu + Nv)}{Su + Sv} \qquad \text{Eq.8}$$

The normalized connectivity measure of each region was then normalized by total normalized connectivity value of each subject to compare across subjects. Finally, the ratio structural connectivity value from bilateral active simulation to six brain regions in each individual was compared. As no method has yet been validated to quantify absolute structural connectivity strengths, the normalized connectivity method was used to evaluate relative

strength within each patient. No comparison of absolute connectivity values are made across subjects.

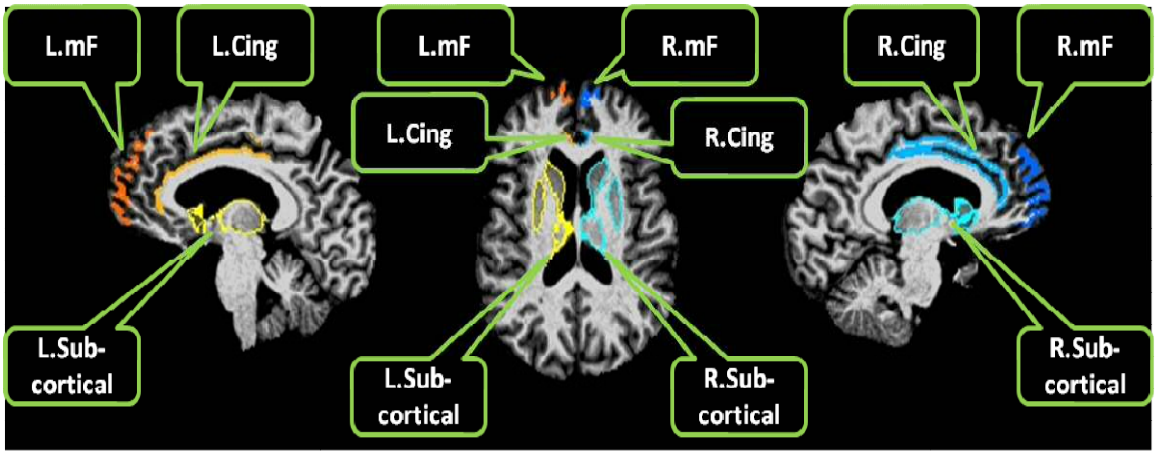

Figure 16. Target regions used for DBS seed-to-target fiber probabilistic tractography maps. Three regions selected from Desikan and Harvard-Oxford atlases: medial frontal cortex, anterior cingulate, and subcortical cluster (Basal ganglia including nucleus accumbens, caudate, putamen, and thalamus). Right and Left sided regions are sampled independently.

(c) Correlation between structural connectivity and clinical efficacy of SCC DBS

To evaluate the relationship between specific tract connectivity and clinical efficacy of DBS treatment, correlations between normalized connectivity values with HDRS-17 scores at 24 weeks and illness density index (IDI) were calculated (200). The IDI, based on an integration of the HDRS-17 scores over the 24 weeks of open, chronic DBS, is a non-categorical, continuous measurement of clinical efficacy of SCC DBS.

4.2.5 Anatomical active stimulation coordinates

Given past attempts using lower resolution MRI data to evaluate anatomical variation in contact locations in responders and non-responders to SCC DBS (13, 163), a final analysis of the activation volume location in standard stereotaxic space using the high resolution pre-surgical T_1 images was performed. This analysis would show if structural anatomy per se could explain response to DBS. The activation volume for each subject was transferred to MNI space using a combination of linear and non-linear transformations (Flirt and Fnirt: FSL); the center of mass of the activation volume (x-,y-,z- and Euclidean-distance from MNI center coordinate) was statistically tested.

4.3. Results

4.3.1. Probabilistic Tractography Analysis

(a) Whole-brain tractography analysis

Three bilateral WM pathways were common to all DBS responders (n=6) : bilateral forceps minor connecting the seed to the medial frontal cortex (Brodmann Area 10), the cingulate bundle connecting the seed to the rostral and dorsal anterior and mid-cingulate cortex, and short subcortical midline fibers to subcortical nuclei including the nucleus accumbens, caudate, putamen and anterior thalamus (Figure 17). To prevent that these connections

are not biased to specific subjects, more than 50 % subjects shared pathways are investigated and shows in Figure 18.

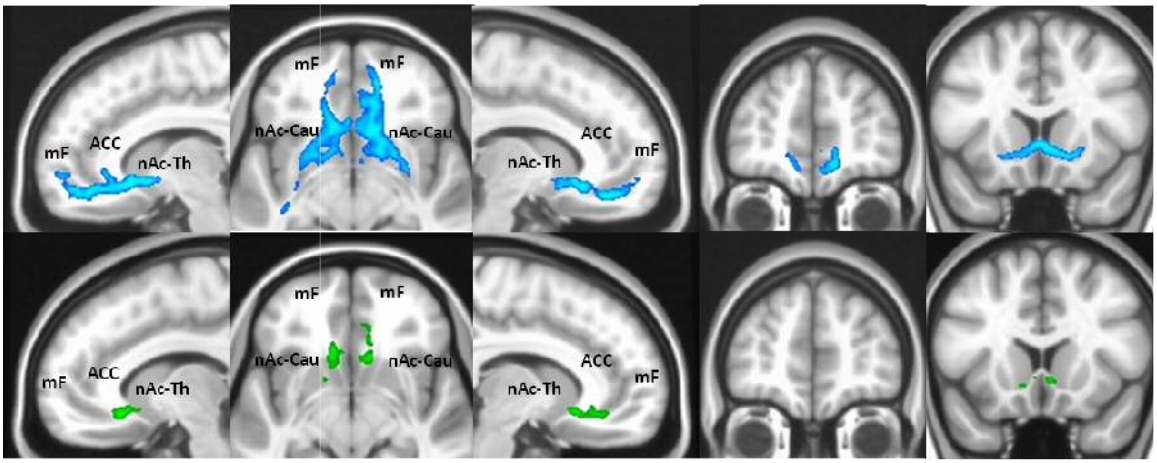

Figure 17. Group Whole-brain probabilistic tractography map defining the optimal DBS fiber tract target. Based on individual activation volume tract maps, all 6-month Responders (Blue) share bilateral pathways to: medial frontal-cortex (BA10) via forceps minor; subgenual, rostral and dorsal anterior cingulate via the cingulum bundle; and to nucleus accumbens, caudate, hypothalamus and anterior thalamus. Common tracts shared by all subjects regardless of 6-month response are shown in green. Abbreviations: mF: medial frontal, nAc: nucleus accumbens, Th: thalamus, Cau: caudate.

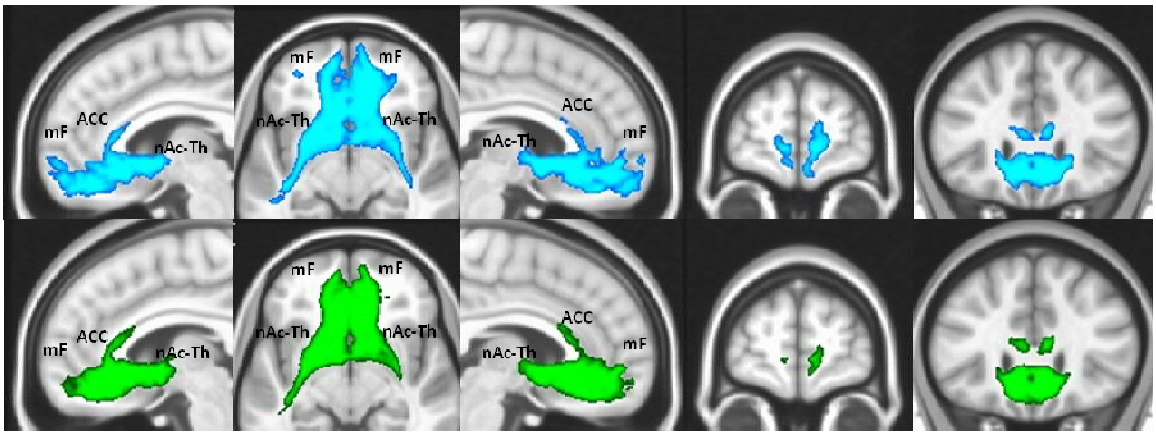

Figure 18. Whole brain fiber probabilistic tractography shared pathways map of more than 50% subjects, Responder group (Blue) shows robust shared pathways to medial frontal and subcortical regions. Green shows the shared pathways of all subjects which include responders and non-responders. Specific shared pathways to bilateral medial frontal were still indentified in responders group.

(b) Seed-to-target tractography analysis

Confirming the findings from the whole brain analysis, DBS responders again showed consistent structural connectivity to both left and right medial frontal cortex (BA10), relative to the non-responders (Table 6). This result is evident in both the total absolute number of threads to each MF region and as a normalized ratio of connectivity comparing all six target regions. Non-responders showed weak structural connectivity to one or both medial frontal cortex regions. The main difference between response and non-response to SCC DBS at 6 months of stimulation is the presence or absence of these strong structural connections to medial frontal lobes *bilaterally*. Structural connectivity of the SCC seed to other regions (subcortical structures, cingulate) was comparable between response groups.

Table 6. Seed-to-Target Analysis: Normalized structural connectivity from bilateral activation volumes to six predefined regions of interest based on the Whole- Brain Connectivity maps.

	Subject	Medial Frontal		Cingulate Cortex		BasalGanglia/Thalamus	
		Left	Right	Left	Right	Left	Right
Responder N.C. (Ratio, %)	1	37.44 (1.85)	169.56 (8.38)	155.87 (7.70)	398.97 (19.71)	482.12 (23.81)	780.49 (38.55)
	2	104.00 (3.65)	133.06 (4.67)	172.55 (6.05)	506.95 (17.78)	1208.60 (42.38)	726.44 (25.47)
	3	28.48 (0.88)	74.47 (2.31)	527.47 (16.37)	614.50 (19.08)	1372.45 (42.60)	604.06 (18.75)
	4	14.76 (0.79)	370.05 (19.69)	110.73 (5.89)	210.59 (11.21)	793.99 (42.25)	379.16 (20.18)
	5	416.54 (14.68)	530.61 (18.70)	416.06 (14.66)	341.42 (12.03)	762.47 (26.87)	370.66 13.06
	6	408.02 (16.69)	280.67 (11.48)	772.14 (31.58)	711.85 (29.11)	106.95 (4.37)	165.76 (6.78)
Non-Responder N.C. (Ratio, %)	1	0.65 (0.33)	0.59 (0.30)	112.86 (57.47)	18.82 (9.58)	46.22 (23.54)	17.25 (8.78)
	2	235.61 (8.75)	1.07 (0.04)	789.67 (29.33)	708.04 (26.29)	684.92 (25.44)	273.41 (10.15)
	3	3.28 (0.16)	161.05 (7.71)	71.39 (3.42)	50.78 (2.43)	1186.06 (56.80)	615.51 (29.48)
	4	1.10 (0.08)	66.45 (4.91)	0.06 (0.00)	0.42 (0.03)	748.26 (55.31)	536.58 (39.66)
	5	1.92 (0.05)	92.13 (2.59)	458.06 (12.90)	2164.69 (60.96)	493.56 (13.90)	340.76 (9.60)
	6	121.32 (2.63)	1.80 0.04	1370.89 29.66	1393.41 30.15	1211.30 26.21	522.56 11.31
	7	3.59 (0.09)	12.28 (0.32)	1206.76 (31.31)	938.19 (24.34)	878.54 (22.79)	815.10 (21.15)
	8	0.06 (0.18)	0.28 (0.89)	0.41 (1.31)	0.37 (1.18)	17.65 (56.51)	12.47 (39.93)
	9	631.19 (14.67)	1097.62 (25.50)	790.40 (18.37)	793.98 (18.45)	854.70 (19.86)	135.87 (3.16)
	10	70.04 (1.53)	253.56 (5.54)	1425.52 (31.17)	1091.02 (23.86)	925.16 (20.23)	807.66 (17.66)

N.C.: Normalized structural connectivity. Gray shade indicates normalized connection value less than 10, indicative of no connection meeting threshold criteria.

(c) Correlation between structural connectivity and clinical efficacy of SCC DBS

HDRS-17 score at 24 weeks Response magnitude across all subjects using the HAMD-17 at six months was significantly correlated with structural connectivity of the SCC to both medial frontal cortices (Spearman's rho, Left mF: $p = 0.035$, Right mF: $p = 0.025$). The Illness Density Index (IDI) was also significantly correlated with structural connectivity of the SCC to both medial frontal cortices in all subjects (Spearman's rho, Left mF: $p = 0.005$, Right mF: $p = 0.025$). Strength of structural connections with the 24-week HDRS-17 or the IDI were not significant for any of the other response-specific pathways (Figure 19).

4.3.2. Anatomical active stimulation coordinate

Anatomical location of the active contacts did not discriminate the subgroups. There were no significant differences between responders and non-responders when analyzing either the coordinates of electrode (activation volumes) or the Euclidean distance from MNI center. (Mann-Whitney U test uncorrected, Left x: $p = 0.32$, y: $p = 0.51$, z: $p = 0.38$, Euclidean distance: $p = 0.58$; Right x: $p = 0.36$, y: $p = 0.63$, z: $p = 0.42$, Euclidean distance: $p = 0.87$) (Figure 19 and Table 7). In addition, there was no lateralized difference in the location of the active contacts in the right and left hemisphere, based on the coordinates of the activation volumes.

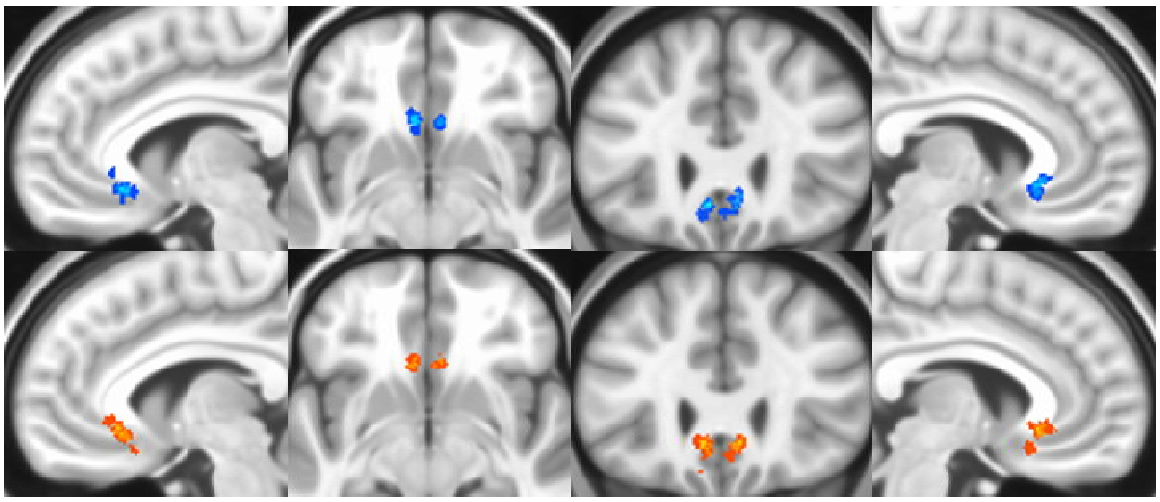

Figure 19. Anatomical location in MNI space of the VAT for responders (Blue) and non-responders (Red) at six months of chronic DBS. There is no differences in anatomical location between the responder and non-responder groups.

Table 7. Coordinates of Activation Volumes in MNI space

	Left hemisphere				Right hemisphere			
	x	y	z	ED	x	y	z	ED
Responder (n=6)	-5.98 (±1.11)	25.61 (±3.02)	-8.11 (±3.69)	27.68 (±2.35)	6.14 (±0.33)	26.21 (±2.12)	-6.04 (±2.21)	27.70 (±1.83)
Non-Responder (n=10)	-6.86 (±1.35)	26.53 (±2.35)	-7.80 (±3.98)	28.77 (±1.73)	5.34 (±1.56)	25.63 (±2.62)	-7.46 (±3.28)	27.48 (±2.20)
Stat. (*p*)	0.32	0.51	0.38	0.58	0.36	0.63	0.42	0.87

ED: Euclidean distance from MNI center coordinate, Stat.: Statistical analysis (Mann-Whitney U test), *p*: p-value .

4.4. Discussion

This study demonstrates that clinical response to DBS is mediated by direct impact on a combination of specific fiber bundles passing through the SCC white matter target. These fiber bundles include: (a) bilateral forceps minor of the anterior corpus callosum connecting the right and left medial frontal cortices, (b) the bilateral cingulum bundles connecting ipsilateral subcallosal cingulate to rostral and dorsal anterior cingulate cortices, and (c) frontal-striatal fibers of the medial branch of the uncinate fasciculus connecting medial frontal and subcallosal cingulate areas to the nucleus accumbens, anterior thalamus and other subcortical regions Involvement of these 3 sets of bundles in each hemisphere is confirmed using three different methods to define structural connectivity of the target. The whole-brain analysis generates a visual "fingerprint" of the full tract target. Secondly, seed-to-target analysis demonstrates the necessary involvement of connections of the SCC to bilateral medial frontal cortices in responders to DBS. The non-responder group missed critical frontal connections and each of them had weak connections to one or both medial frontal lobes. Thirdly, in addition to describing the necessary pathways for optimal response, a linear correlation is seen between connectivity of the target activation volumes to bilateral medial frontal lobes and treatment response.

The implementation of patient- and contact-specific electrical field modeling in conjunction with tractography allows a new insight into the way DBS mediates antidepressant response with implications for patient management. Previous reports of

anatomical location of contacts failed to explain why some participants did not respond to SCC DBS (163); a finding also confirmed in this cohort (Figure 19). These new data provide insight into an alternative key source of variability, namely the impact on multiple fiber bundles as pass through this region of the SCC.

While these findings provide a potential strategy for optimizing DBS lead placement, the sample size is small, and a replication cohort with prospective testing is needed. Additionally, improved DTI acquisition methods (201), may allow detection of more subtle but equally critical pathways mediating response to SCC DBS such as pathways to the brainstem or medial branches of the uncinate fasciculus which sits lateral to forceps minor at this axial plane (187).

Based on the combined analyses in this study, it might be postulated that targeting bilateral SCC-Brodmann Area 10 (medial frontal cortex) connections alone might be sufficient to generate the optimal antidepressant effect as these tracts best distinguish responders and non-responders among the constellation of tracts identified and correlated with indices of clinical response across all subjects. However, with current DBS systems, and the associated size and shape of the stimulation field, specific stimulation of SCC-BA10 fibers is not possible; cingulate and subcortical connections will also be stimulated. Future studies with capacity for current steering may allow direct testing of this hypothesis (202). Such technological advances will also allow disambiguation of stimulation of the direct SCC-BA10 connections from trans-hemispheric connections through forceps minor and even passing fibers from mF10 to subcortical regions.

The primary finding from this study is that antidepressant effects of chronic high frequency DBS likely involves modulation of a distributed network in addition to local changes in SCC grey matter. Based on the available evidence, the mechanisms of DBS most likely involve a combination of local effects on neurons and glia in the direct current field with secondary transynaptic effects as well as orthodromic and antidromic effects on fibers of passage (203, 204). Full characterization of the fiber and cell types will be required to model DBS mechanisms of action.

Clinically, this network analysis provides a potential new algorithm for target selection for SCC DBS. Instead of a purely anatomical or coordinate based approach that targets a single region, these findings suggest that targeting be based on connectivity within the network, i.e., which target will allow for a stimulation field that impacts the critical local regions and the white matter tracts to other key regions within the network. This can be prospectively tested using a pre-surgical assessment of an individual patient's network structure with lead placement and contact selection done to ensure a current field that impacts the three white matter bundles described here.

Management of non-responders to SCC DBS in this context is an important next consideration. Non-response can be multifactorial: inadequate patient selection, personality characteristics, psychological or environmental factors that become evident after the implantation in addition to missed pathways. As such, the lack of a full DBS response may be independent of appropriate modulation of the requisite neural pathways.

Therefore, we propose that contacts should not be changed prematurely if the individual connectivity map showed the tracts that matched the desired response "fingerprint". This hypothesis will be tested in future analyses of the non-responder group.

In conclusion, the tractography maps of unambiguous response to chronic SCC DBS define a template involving bilateral forceps minor, cingulum and medial frontal-striatal/subcortical fibers which may be characterized in individual patients prior to surgery using probabilistic tractography. Such an approach provides a new strategy for optimizing electrode implantation for SCC DBS.

CHAPTER 5

Conclusions and Future Directions

5.1 Problem Statement

Diffusion tensor imaging is becoming more commonly applied to explore the neurobiology of depression, and methods that study WM integrity need to be validated and quantified (Chapter 2). We described in previous chapters that measuring and identifying the structural neural circuits of depression using network analysis can provide additional information of neuronal alteration of the networks associated with depression (Chapter 3). Diffusion tractography has been used in recent research to analyze brain circuits that are associated with antidepressant response, possibly improving efficacy of subcallosal cingulate deep brain stimulation by defining necessary WM pathways (Chapter 4).

5.2 Overview of Findings

This work has focused on neural circuits of depression in order to clarify and further extend past observations that have been reported in in MDD. The methods we have described could potentially be utilized to optimize targeting of SCC deep brain

stimulation in patients with treatment-resistant depression, by utilizing the WM network analysis in MDD.

Through evaluation of a comprehensive set of analyses for structural WM integrity in a large sample of depressed patients, we demonstrated that disruption of WM does not play a major role in the neurobiology of MDD (Chapter 2).

Using graph theory analysis to assess the organization of neural networks in MDD, we elucidated the importance of WM network, especially alteration of topological organization in MDD (Chapter 3). As an extension of this WM network analysis, we identified the necessary and sufficient WM circuits that are associated with antidepressant response in deep brain stimulation of the subcallosal cingulate cortex for treatment of depression. Clinical efficacy of DBS could be positively impacted by more precise targeting of these necessary tracts.

5.3 Future Directions

Current SCC DBS targeting is based on coordinates that rely on structural T1- and T2-weighted imaging.(163). Target location for lead implantation and choice of active contacts for stimulation are purely based on T_1-weighted MR imaging, interpreted by the psychiatrists and neurosurgeons. . This method of target selection may explain some of the variability of clinical outcomes in SCC DBS.

Assessment of Structural Connectivity from active stimulation contacts through the key therapeutic contacts has not been done to date in SCC DBS. This novel approach to analyzing SCC DBS connections will help create a systematic approach for prospective target selection as well as optimizing contact selection in subjects who are already implanted and are receiving chronic DBS with suboptimal response. Slight variations in the anatomical location of stimulation can produce very different behavioral effects and this variation appears related to the precise combination of key therapeutic tracts affected by the stimulation (190). Therefore, as small changes in the target of stimulation have clinically significant behavioral effects, better understanding of the connectivity patterns of different targets within the SCC region is a critical next step.

DBS electrode placement in the SCC could be optimized by incorporating the identification of critical WM tracts before surgery. In order to develop a systematic target selection procedure using tractography, a qualitative approach could be easily tested prior to surgery. A priori identification of these tracts has been done in subjects who received DBS in the SCC, as described in chapter 4.

For this qualitative target selection, deterministic tractography was performed by using TrackVis (Wang R, Wedeen VJ, MGH) toolbox to find similarly desired connection patterns to key WM tracts that were defined in previous chapter. A tract density map was calculated using Diffusion Toolkit (Dtk, Wang R, Wedeen VJ, MGH) and then bilateral ROIs of 2.5 mm radius sphere-shape were initially placed in SCC region based on brain anatomy. The size of the radius was chosen given that the average

size of volume of activated tissue (VAT) was around 70 mm^3 in previous analysis (Chapter 4). Following this, the tracts passing through bilateral initial seeds were analyzed along user-interactive changes of seed location in SCC region to determine the selected seed location that they connected to the identified regions in the previous chapter (e.g. bilateral mF10, ACC, sub-cortical cluster including striatum, thalamus, nucleus accumbens). This target selection was performed by both neuro-psychiatrists and neurosurgeons. An example of this qualitative individual target selection with deterministic tractography is shown in Figure 20. In order to compare differences in efficacy between purely structural anatomical approach and prospective tract identification, a sample of 27 participants in an ongoing protocol for SCC DBS was analyzed. The initial 17 patients in the sample were implanted based on the classical anatomical target selection, and ten subjects were implanted after DTI-based method target selection was used. By using tractography-based qualitative DTI target selection, clinical response (as defined by a 50 % improvement in Hamilton Depression Rating Scale – 17 item) after six months of chronic stimulation was improved from original 41% (7 responders out of 17 participants) (15) to 70% (7 responders out of 10 participants). This result is suggestive of the improved efficacy of SCC when using quantitative DTI target selection approach.

For quantitative DTI target selection based on probabilistic tractography, normalized connectivity (described in chapter 4) was used. Optimal quantitative target location was suggested by identification of the voxel that has the highest normalized

connectivity value to six previously defined tracts. Preliminary results are shown in Figure 21.

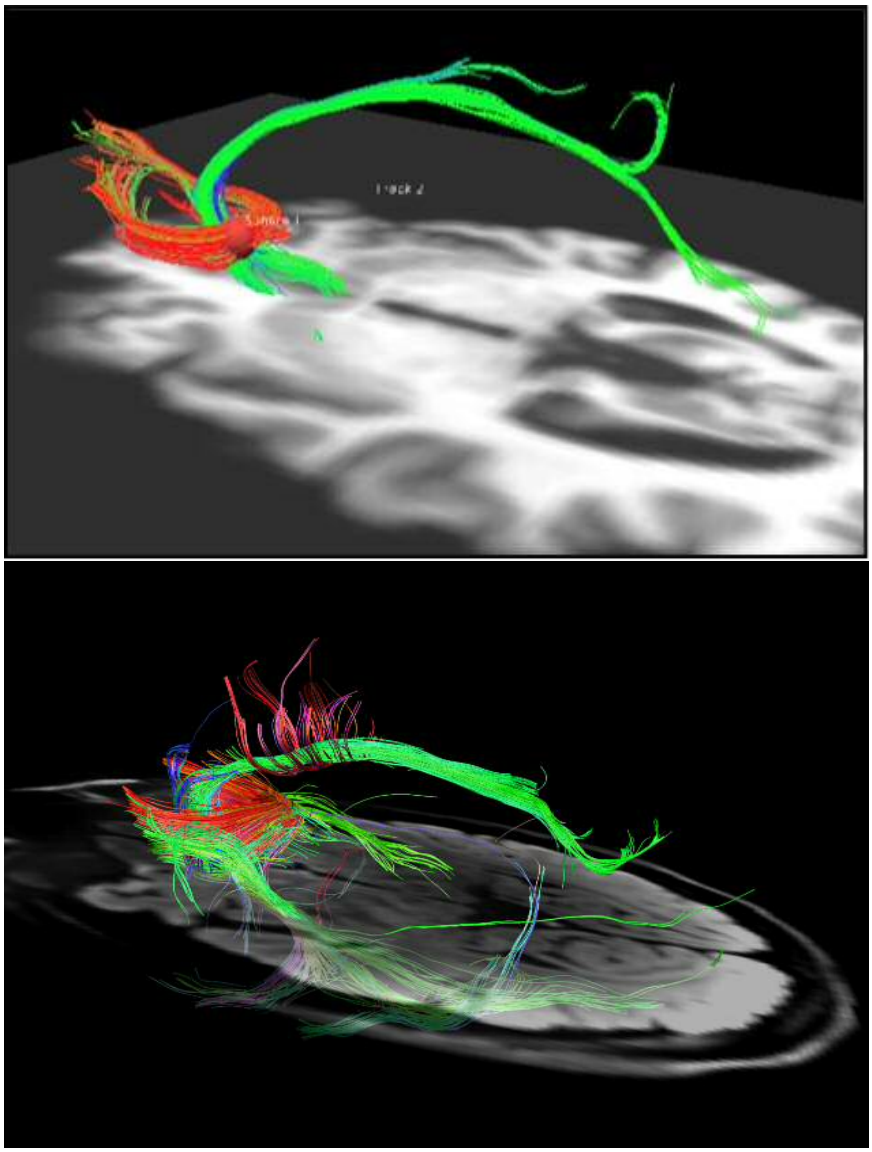

Figure 20. Qualitative DTI target selection using deterministic tractography, Top: Applied restricted (<35 degree) angular threshold for tracking, Bottom: < 90 degree angular threshold for tracking.

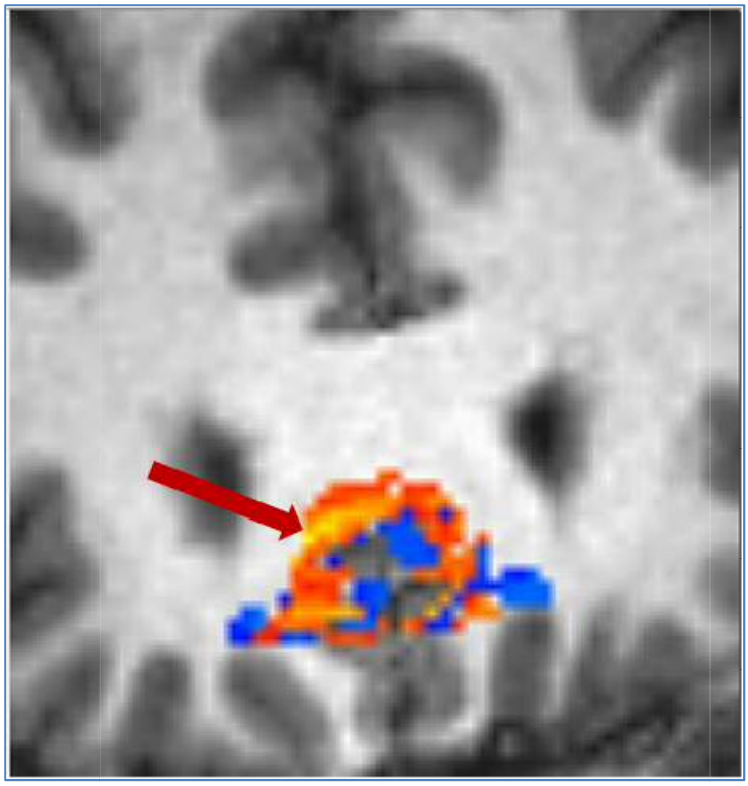

Figure 21. Preliminary result for quantitative DTI target selection using probabilistic tractography, Red arrow indicated the voxel has highest normalized connectivity value to six indentified key tracts.

The preliminary outcomes described above can be related to other factors independent of target selection (patient selection, environmental factors) the improved efficacy could be accounted by the use of these qualitative and quantitative DTI-based tractography target selection. Even more encouraging is the suggestion of improved outcomes by developing a systematical DTI target selection.

In the future, implementation of prospective DTI target selection will improve surgical precision, minimize unnecessary stimulation parameter modifications and set a new standard for effective SCC DBS. This will be tested with upcoming DBS surgeries.

REFERENCES

1. Zhu X, Wang X, Xiao J, Zhong M, Liao J, Yao S (2011): Altered white matter integrity in first-episode, treatment-naive young adults with major depressive disorder: a tract-based spatial statistics study. *Brain research*. 1369:223-229.

2. Wu F, Tang Y, Xu K, Kong L, Sun W, Wang F, et al. (2011): Whiter matter abnormalities in medication-naive subjects with a single short-duration episode of major depressive disorder. *Psychiatry research*. 191:80-83.

3. Abe O, Takao H, Gonoi W, Sasaki H, Murakami M, Kabasawa H, et al. (2010): Voxel-based analysis of the diffusion tensor. *Neuroradiology*. 52:699-710.

4. Kieseppa T, Eerola M, Mantyla R, Neuvonen T, Poutanen VP, Luoma K, et al. (2010): Major depressive disorder and white matter abnormalities: a diffusion tensor imaging study with tract-based spatial statistics. *Journal of affective disorders*. 120:240-244.

5. Cullen KR, Klimes-Dougan B, Muetzel R, Mueller BA, Camchong J, Houri A, et al. (2010): Altered white matter microstructure in adolescents with major depression: a preliminary study. *Journal of the American Academy of Child and Adolescent Psychiatry*. 49:173-183 e171.

6. Korgaonkar MS, Grieve SM, Koslow SH, Gabrieli JD, Gordon E, Williams LM (2011): Loss of white matter integrity in major depressive disorder: evidence using tract-based spatial statistical analysis of diffusion tensor imaging. *Human brain mapping*. 32:2161-2171.

7. Blood AJ, Iosifescu DV, Makris N, Perlis RH, Kennedy DN, Dougherty DD, et al. (2010): Microstructural abnormalities in subcortical reward circuitry of subjects with major depressive disorder. *PloS one*. 5:e13945.

8. Zou K, Huang X, Li T, Gong Q, Li Z, Ou-yang L, et al. (2008): Alterations of white matter integrity in adults with major depressive disorder: a magnetic resonance imaging study. *Journal of psychiatry & neuroscience : JPN*. 33:525-530.

9. Ma N, Li L, Shu N, Liu J, Gong G, He Z, et al. (2007): White matter abnormalities in first-episode, treatment-naive young adults with major depressive disorder. *The American journal of psychiatry*. 164:823-826.

10. Cole J, Chaddock CA, Farmer AE, Aitchison KJ, Simmons A, McGuffin P, et al. (2012): White matter abnormalities and illness severity in major depressive disorder. *The British journal of psychiatry : the journal of mental science*. 201:33-39.

11. Tha KK, Terae S, Nakagawa S, Inoue T, Kitagawa N, Kako Y, et al. (2013): Impaired integrity of the brain parenchyma in non-geriatric patients with major depressive disorder revealed by diffusion tensor imaging. *Psychiatry research*. 212:208-215.

12. Mayberg HS, Lozano AM, Voon V, McNeely HE, Seminowicz D, Hamani C, et al. (2005): Deep brain stimulation for treatment-resistant depression. *Neuron*. 45:651-660.

13. Johansen-Berg H, Gutman DA, Behrens TE, Matthews PM, Rushworth MF, Katz E, et al. (2008): Anatomical connectivity of the subgenual cingulate region targeted with deep brain stimulation for treatment-resistant depression. *Cerebral cortex*. 18:1374-1383.

14. Gutman DA, Holtzheimer PE, Behrens TE, Johansen-Berg H, Mayberg HS (2009): A tractography analysis of two deep brain stimulation white matter targets for depression. *Biological psychiatry*. 65:276-282.

15. Holtzheimer PE, Kelley ME, Gross RE, Filkowski MM, Garlow SJ, Barrocas A, et al. (2012): Subcallosal cingulate deep brain stimulation for treatment-resistant unipolar and bipolar depression. *Archives of general psychiatry*. 69:150-158.

16. Basser PJ, Mattiello J, LeBihan D (1994): Estimation of the effective self-diffusion tensor from the NMR spin echo. *Journal of magnetic resonance Series B*. 103:247-254.

17. Le Bihan D, Mangin JF, Poupon C, Clark CA, Pappata S, Molko N, et al. (2001): Diffusion tensor imaging: concepts and applications. *Journal of magnetic resonance imaging : JMRI*. 13:534-546.

18. Mori S *Introduction to Diffusion Tensor Imaging*. ELSEVIER.

19. Mori S, Zhang J (2006): Principles of diffusion tensor imaging and its applications to basic neuroscience research. *Neuron*. 51:527-539.

20. Heidi Johansen-Berg TEJB *Diffusion MRI: From quantitative measurement to in vivo neuroanatomy*. ACAMEMIC PRESS.

21. Kubicki M, Westin CF, Maier SE, Mamata H, Frumin M, Ersner-Hershfield H, et al. (2002): Diffusion tensor imaging and its application to neuropsychiatric disorders. *Harvard review of psychiatry*. 10:324-336.

22. Savitz JB, Rauch SL, Drevets WC (2013): Clinical application of brain imaging for the diagnosis of mood disorders: the current state of play. *Molecular psychiatry*. 18:528-539.

23. Basser PJ, Mattiello J, LeBihan D (1994): MR diffusion tensor spectroscopy and imaging. *Biophysical journal*. 66:259-267.

24. Pierpaoli C, Basser PJ (1996): Toward a quantitative assessment of diffusion anisotropy. *Magnetic resonance in medicine : official journal of the Society of Magnetic Resonance in Medicine / Society of Magnetic Resonance in Medicine*. 36:893-906.

25. Song SK, Sun SW, Ramsbottom MJ, Chang C, Russell J, Cross AH (2002): Dysmyelination revealed through MRI as increased radial (but unchanged axial) diffusion of water. *NeuroImage*. 17:1429-1436.

26. Basser PJ, Pajevic S, Pierpaoli C, Duda J, Aldroubi A (2000): In vivo fiber tractography using DT-MRI data. *Magnetic resonance in medicine : official journal of the Society of Magnetic Resonance in Medicine / Society of Magnetic Resonance in Medicine*. 44:625-632.

27. White T, Nelson M, Lim KO (2008): Diffusion tensor imaging in psychiatric disorders. *Topics in magnetic resonance imaging : TMRI*. 19:97-109.

28. Shizukuishi T, Abe O, Aoki S (2013): Diffusion Tensor Imaging Analysis for Psychiatric Disorders. *Magnetic resonance in medical sciences : MRMS : an official journal of Japan Society of Magnetic Resonance in Medicine*.

29. McKenna MT, Michaud CM, Murray CJ, Marks JS (2005): Assessing the burden of disease in the United States using disability-adjusted life years. *American journal of preventive medicine*. 28:415-423.

30. Kessler RC, Berglund P, Demler O, Jin R, Koretz D, Merikangas KR, et al. (2003): The epidemiology of major depressive disorder: results from the National Comorbidity Survey Replication (NCS-R). *JAMA : the journal of the American Medical Association*. 289:3095-3105.

31. Mayberg HS (2009): Targeted electrode-based modulation of neural circuits for depression. *The Journal of clinical investigation*. 119:717-725.

32. Drevets WC, Price JL, Furey ML (2008): Brain structural and functional abnormalities in mood disorders: implications for neurocircuitry models of depression. *Brain structure & function*. 213:93-118.

33. Gotlib IH, Joormann J (2010): Cognition and depression: current status and future directions. *Annual review of clinical psychology*. 6:285-312.

34. Sacher J, Neumann J, Funfstuck T, Soliman A, Villringer A, Schroeter ML (2012): Mapping the depressed brain: a meta-analysis of structural and functional alterations in major depressive disorder. *Journal of affective disorders*. 140:142-148.

35. Mayberg HS, Liotti M, Brannan SK, McGinnis S, Mahurin RK, Jerabek PA, et al. (1999): Reciprocal limbic-cortical function and negative mood: converging PET findings in depression and normal sadness. *The American journal of psychiatry*. 156:675-682.

36. Lui S, Parkes LM, Huang X, Zou K, Chan RC, Yang H, et al. (2009): Depressive disorders: focally altered cerebral perfusion measured with arterial spin-labeling MR imaging. *Radiology*. 251:476-484.

37. Gilbert AM, Prasad K, Goradia D, Nutche J, Keshavan M, Frank E (2010): Grey matter volume reductions in the emotion network of patients with depression and coronary artery disease. *Psychiatry research*. 181:9-14.

38. Frodl T, Scheuerecker J, Albrecht J, Kleemann AM, Muller-Schunk S, Koutsouleris N, et al. (2009): Neuronal correlates of emotional processing in patients with major depression. *The world journal of biological psychiatry : the official journal of the World Federation of Societies of Biological Psychiatry*. 10:202-208.

39. Lemogne C, le Bastard G, Mayberg H, Volle E, Bergouignan L, Lehericy S, et al. (2009): In search of the depressive self: extended medial prefrontal network during self-

referential processing in major depression. *Social cognitive and affective neuroscience*. 4:305-312.

40. Hamilton JP, Siemer M, Gotlib IH (2008): Amygdala volume in major depressive disorder: a meta-analysis of magnetic resonance imaging studies. *Molecular psychiatry*. 13:993-1000.

41. Hamilton JP, Etkin A, Furman DJ, Lemus MG, Johnson RF, Gotlib IH (2012): Functional neuroimaging of major depressive disorder: a meta-analysis and new integration of base line activation and neural response data. *The American journal of psychiatry*. 169:693-703.

42. Ashburner J, Friston KJ (2000): Voxel-based morphometry--the methods. *NeuroImage*. 11:805-821.

43. Good CD, Johnsrude IS, Ashburner J, Henson RN, Friston KJ, Frackowiak RS (2001): A voxel-based morphometric study of ageing in 465 normal adult human brains. *NeuroImage*. 14:21-36.

44. Smith SM, Jenkinson M, Johansen-Berg H, Rueckert D, Nichols TE, Mackay CE, et al. (2006): Tract-based spatial statistics: voxelwise analysis of multi-subject diffusion data. *NeuroImage*. 31:1487-1505.

45. Smith SM, Johansen-Berg H, Jenkinson M, Rueckert D, Nichols TE, Miller KL, et al. (2007): Acquisition and voxelwise analysis of multi-subject diffusion data with tract-based spatial statistics. *Nature protocols*. 2:499-503.

46. Li L, Coles CD, Lynch ME, Hu X (2009): Voxelwise and skeleton-based region of interest analysis of fetal alcohol syndrome and fetal alcohol spectrum disorders in young adults. *Human brain mapping*. 30:3265-3274.

47. Xie S, Xiao JX, Gong GL, Zang YF, Wang YH, Wu HK, et al. (2006): Voxel-based detection of white matter abnormalities in mild Alzheimer disease. *Neurology*. 66:1845-1849.

48. Bae JN, MacFall JR, Krishnan KR, Payne ME, Steffens DC, Taylor WD (2006): Dorsolateral prefrontal cortex and anterior cingulate cortex white matter alterations in late-life depression. *Biological psychiatry*. 60:1356-1363.

49. Mayberg HS (2003): Positron emission tomography imaging in depression: a neural systems perspective. *Neuroimaging clinics of North America*. 13:805-815.

50. Mayberg HS (2003): Modulating dysfunctional limbic-cortical circuits in depression: towards development of brain-based algorithms for diagnosis and optimised treatment. *British medical bulletin*. 65:193-207.

51. Phillips ML (2006): The neural basis of mood dysregulation in bipolar disorder. *Cognitive neuropsychiatry*. 11:233-249.

52. Hafeman DM, Chang KD, Garrett AS, Sanders EM, Phillips ML (2012): Effects of medication on neuroimaging findings in bipolar disorder: an updated review. *Bipolar disorders*. 14:375-410.

53. Drevets WC, Savitz J, Trimble M (2008): The subgenual anterior cingulate cortex in mood disorders. *CNS spectrums*. 13:663-681.

54. Murray EA, Wise SP, Drevets WC (2011): Localization of dysfunction in major depressive disorder: prefrontal cortex and amygdala. *Biological psychiatry*. 69:e43-54.

55. James GA, Kelley ME, Craddock RC, Holtzheimer PE, Dunlop BW, Nemeroff CB, et al. (2009): Exploratory structural equation modeling of resting-state fMRI: applicability of group models to individual subjects. *NeuroImage*. 45:778-787.

56. Craddock RC, Holtzheimer PE, 3rd, Hu XP, Mayberg HS (2009): Disease state prediction from resting state functional connectivity. *Magnetic resonance in medicine : official journal of the Society of Magnetic Resonance in Medicine / Society of Magnetic Resonance in Medicine*. 62:1619-1628.

57. Craddock RC, James GA, Holtzheimer PE, 3rd, Hu XP, Mayberg HS (2012): A whole brain fMRI atlas generated via spatially constrained spectral clustering. *Human brain mapping*. 33:1914-1928.

58. Seminowicz DA, Mayberg HS, McIntosh AR, Goldapple K, Kennedy S, Segal Z, et al. (2004): Limbic-frontal circuitry in major depression: a path modeling metanalysis. *NeuroImage*. 22:409-418.

59. Greicius MD, Flores BH, Menon V, Glover GH, Solvason HB, Kenna H, et al. (2007): Resting-state functional connectivity in major depression: abnormally increased contributions from subgenual cingulate cortex and thalamus. *Biological psychiatry*. 62:429-437.

60. Greicius M (2008): Resting-state functional connectivity in neuropsychiatric disorders. *Current opinion in neurology*. 21:424-430.

61. Sheline YI, Price JL, Yan Z, Mintun MA (2010): Resting-state functional MRI in depression unmasks increased connectivity between networks via the dorsal nexus. *Proceedings of the National Academy of Sciences of the United States of America*. 107:11020-11025.

62. Rykhlevskaia E, Gratton G, Fabiani M (2008): Combining structural and functional neuroimaging data for studying brain connectivity: a review. *Psychophysiology*. 45:173-187.

63. Greicius MD, Supekar K, Menon V, Dougherty RF (2009): Resting-state functional connectivity reflects structural connectivity in the default mode network. *Cerebral cortex*. 19:72-78.

64. Guye M, Bartolomei F, Ranjeva JP (2008): Imaging structural and functional connectivity: towards a unified definition of human brain organization? *Current opinion in neurology*. 21:393-403.

65. Guye M, Bettus G, Bartolomei F, Cozzone PJ (2010): Graph theoretical analysis of structural and functional connectivity MRI in normal and pathological brain networks. *MAGMA*. 23:409-421.

66. Sharp DJ, Beckmann CF, Greenwood R, Kinnunen KM, Bonnelle V, De Boissezon X, et al. (2011): Default mode network functional and structural connectivity after traumatic brain injury. *Brain : a journal of neurology*. 134:2233-2247.

67. Sporns O (2011): The human connectome: a complex network. *Annals of the New York Academy of Sciences*. 1224:109-125.

68. Dale AM, Fischl B, Sereno MI (1999): Cortical surface-based analysis. I. Segmentation and surface reconstruction. *NeuroImage*. 9:179-194.

69. Lo CY, Wang PN, Chou KH, Wang J, He Y, Lin CP (2010): Diffusion tensor tractography reveals abnormal topological organization in structural cortical networks in Alzheimer's disease. *The Journal of neuroscience : the official journal of the Society for Neuroscience*. 30:16876-16885.

70. van den Heuvel MP, Mandl RC, Stam CJ, Kahn RS, Hulshoff Pol HE (2010): Aberrant frontal and temporal complex network structure in schizophrenia: a graph theoretical analysis. *The Journal of neuroscience : the official journal of the Society for Neuroscience*. 30:15915-15926.

71. He Y, Dagher A, Chen Z, Charil A, Zijdenbos A, Worsley K, et al. (2009): Impaired small-world efficiency in structural cortical networks in multiple sclerosis associated with white matter lesion load. *Brain : a journal of neurology*. 132:3366-3379.

72. Olanow CW, Brin MF, Obeso JA (2000): The role of deep brain stimulation as a surgical treatment for Parkinson's disease. *Neurology*. 55:S60-66.

73. Benabid AL, Pollak P, Gao D, Hoffmann D, Limousin P, Gay E, et al. (1996): Chronic electrical stimulation of the ventralis intermedius nucleus of the thalamus as a treatment of movement disorders. *Journal of neurosurgery*. 84:203-214.

74. Vidailhet M, Pollak P (2005): Deep brain stimulation for dystonia: make the lame walk. *Annals of neurology*. 57:613-614.

75. Greenberg BD, Rauch SL, Haber SN (2010): Invasive circuitry-based neurotherapeutics: stereotactic ablation and deep brain stimulation for OCD. *Neuropsychopharmacology : official publication of the American College of Neuropsychopharmacology*. 35:317-336.

76. Lockman J, Fisher RS (2009): Therapeutic brain stimulation for epilepsy. *Neurologic clinics*. 27:1031-1040.

77. Lozano AM, Mayberg HS, Giacobbe P, Hamani C, Craddock RC, Kennedy SH (2008): Subcallosal cingulate gyrus deep brain stimulation for treatment-resistant depression. *Biological psychiatry*. 64:461-467.

78. Malone DA, Jr., Dougherty DD, Rezai AR, Carpenter LL, Friehs GM, Eskandar EN, et al. (2009): Deep brain stimulation of the ventral capsule/ventral striatum for treatment-resistant depression. *Biological psychiatry*. 65:267-275.

79. McNeal DR (1976): Analysis of a model for excitation of myelinated nerve. *IEEE transactions on bio-medical engineering*. 23:329-337.

80. Rattay F (1986): Analysis of models for external stimulation of axons. *IEEE transactions on bio-medical engineering*. 33:974-977.

81. McIntyre CC, Savasta M, Walter BL, Vitek JL (2004): How does deep brain stimulation work? Present understanding and future questions. *Journal of clinical neurophysiology : official publication of the American Electroencephalographic Society*. 21:40-50.

82. Butson CR, Cooper SE, Henderson JM, McIntyre CC (2006): Predicting the effects of deep brain stimulation with diffusion tensor based electric field models. *Medical image computing and computer-assisted intervention : MICCAI International Conference on Medical Image Computing and Computer-Assisted Intervention*. 9:429-437.

83. Dunlop BW, Binder EB, Cubells JF, Goodman MG, Kelley ME, Kinkead B, et al. (2012): Predictors of Remission in Depression to Individual and Combined Treatments (PReDICT): Study Protocol for a Randomized Controlled Trial. *Trials*. 13:106.

84. Dunlop BW, Kelley ME, Mletzko TC, Velasquez CM, Craighead WE, Mayberg HS (2012): Depression beliefs, treatment preference, and outcomes in a randomized trial for major depressive disorder. *Journal of psychiatric research*. 46:375-381.

85. Griswold MA, Jakob PM, Heidemann RM, Nittka M, Jellus V, Wang J, et al. (2002): Generalized autocalibrating partially parallel acquisitions (GRAPPA). *Magnetic resonance in medicine : official journal of the Society of Magnetic Resonance in Medicine / Society of Magnetic Resonance in Medicine*. 47:1202-1210.

86. Smith SM, Jenkinson M, Woolrich MW, Beckmann CF, Behrens TE, Johansen-Berg H, et al. (2004): Advances in functional and structural MR image analysis and implementation as FSL. *NeuroImage*. 23 Suppl 1:S208-219.

87. Andersson JL, Skare S, Ashburner J (2003): How to correct susceptibility distortions in spin-echo echo-planar images: application to diffusion tensor imaging. *NeuroImage*. 20:870-888.

88. Jenkinson M, Bannister P, Brady M, Smith S (2002): Improved optimization for the robust and accurate linear registration and motion correction of brain images. *NeuroImage*. 17:825-841.

89. Behrens TE, Woolrich MW, Jenkinson M, Johansen-Berg H, Nunes RG, Clare S, et al. (2003): Characterization and propagation of uncertainty in diffusion-weighted MR imaging. *Magnetic resonance in medicine : official journal of the Society of Magnetic Resonance in Medicine / Society of Magnetic Resonance in Medicine*. 50:1077-1088.

90. Bullmore ET, Suckling J, Overmeyer S, Rabe-Hesketh S, Taylor E, Brammer MJ (1999): Global, voxel, and cluster tests, by theory and permutation, for a difference between two groups of structural MR images of the brain. *IEEE transactions on medical imaging*. 18:32-42.

91. Wu M, Chang LC, Walker L, Lemaitre H, Barnett AS, Marenco S, et al. (2008): Comparison of EPI distortion correction methods in diffusion tensor MRI using a novel framework. *Medical image computing and computer-assisted intervention : MICCAI International Conference on Medical Image Computing and Computer-Assisted Intervention*. 11:321-329.

92. Huang H, Ceritoglu C, Li X, Qiu A, Miller MI, van Zijl PC, et al. (2008): Correction of B0 susceptibility induced distortion in diffusion-weighted images using large-deformation diffeomorphic metric mapping. *Magnetic resonance imaging*. 26:1294-1302.

93. Oouchi H, Yamada K, Sakai K, Kizu O, Kubota T, Ito H, et al. (2007): Diffusion anisotropy measurement of brain white matter is affected by voxel size: underestimation occurs in areas with crossing fibers. *AJNR American journal of neuroradiology*. 28:1102-1106.

94. Rajkowska G (2003): Depression: what we can learn from postmortem studies. *The Neuroscientist : a review journal bringing neurobiology, neurology and psychiatry*. 9:273-284.

95. Harrison PJ (2002): The neuropathology of primary mood disorder. *Brain : a journal of neurology*. 125:1428-1449.

96. Ongur D, Heckers S (2004): A role for glia in the action of electroconvulsive therapy. *Harvard review of psychiatry*. 12:253-262.

97. Sporns O, Tononi G, Kotter R (2005): The human connectome: A structural description of the human brain. *PLoS computational biology*. 1:e42.

98. Hagmann P, Cammoun L, Gigandet X, Meuli R, Honey CJ, Wedeen VJ, et al. (2008): Mapping the structural core of human cerebral cortex. *PLoS biology*. 6:e159.

99. Gong G, Rosa-Neto P, Carbonell F, Chen ZJ, He Y, Evans AC (2009): Age- and gender-related differences in the cortical anatomical network. *The Journal of neuroscience : the official journal of the Society for Neuroscience*. 29:15684-15693.

100. van den Heuvel MP, Sporns O (2011): Rich-club organization of the human connectome. *The Journal of neuroscience : the official journal of the Society for Neuroscience*. 31:15775-15786.

101. Bullmore E, Sporns O (2009): Complex brain networks: graph theoretical analysis of structural and functional systems. *Nature reviews Neuroscience*. 10:186-198.

102. Bassett DS, Bullmore ET (2009): Human brain networks in health and disease. *Current opinion in neurology*. 22:340-347.

103. He Y, Evans A (2010): Graph theoretical modeling of brain connectivity. *Current opinion in neurology*. 23:341-350.

104. Rubinov M, Sporns O (2010): Complex network measures of brain connectivity: uses and interpretations. *NeuroImage*. 52:1059-1069.

105. Stam CJ (2010): Characterization of anatomical and functional connectivity in the brain: a complex networks perspective. *International journal of psychophysiology : official journal of the International Organization of Psychophysiology*. 77:186-194.

106. Hagmann P, Kurant M, Gigandet X, Thiran P, Wedeen VJ, Meuli R, et al. (2007): Mapping human whole-brain structural networks with diffusion MRI. *PloS one*. 2:e597.

107. He Y, Chen Z, Evans A (2008): Structural insights into aberrant topological patterns of large-scale cortical networks in Alzheimer's disease. *The Journal of neuroscience : the official journal of the Society for Neuroscience*. 28:4756-4766.

108. Supekar K, Menon V, Rubin D, Musen M, Greicius MD (2008): Network analysis of intrinsic functional brain connectivity in Alzheimer's disease. *PLoS computational biology*. 4:e1000100.

109. Stam CJ, de Haan W, Daffertshofer A, Jones BF, Manshanden I, van Cappellen van Walsum AM, et al. (2009): Graph theoretical analysis of magnetoencephalographic functional connectivity in Alzheimer's disease. *Brain : a journal of neurology*. 132:213-224.

110. Yu Q, Sui J, Rachakonda S, He H, Gruner W, Pearlson G, et al. (2011): Altered topological properties of functional network connectivity in schizophrenia during resting state: a small-world brain network study. *PloS one*. 6:e25423.

111. He H, Sui J, Yu Q, Turner JA, Ho BC, Sponheim SR, et al. (2012): Altered small-world brain networks in schizophrenia patients during working memory performance. *PloS one*. 7:e38195.

112. Zalesky A, Fornito A, Seal ML, Cocchi L, Westin CF, Bullmore ET, et al. (2011): Disrupted axonal fiber connectivity in schizophrenia. *Biological psychiatry*. 69:80-89.

113. Leistedt SJ, Coumans N, Dumont M, Lanquart JP, Stam CJ, Linkowski P (2009): Altered sleep brain functional connectivity in acutely depressed patients. *Human brain mapping*. 30:2207-2219.

114. Zhang J, Wang J, Wu Q, Kuang W, Huang X, He Y, et al. (2011): Disrupted brain connectivity networks in drug-naive, first-episode major depressive disorder. *Biological psychiatry*. 70:334-342.

115. Jin C, Gao C, Chen C, Ma S, Netra R, Wang Y, et al. (2011): A preliminary study of the dysregulation of the resting networks in first-episode medication-naive adolescent depression. *Neuroscience letters*. 503:105-109.

116. Singh MK, Kesler SR, Hadi Hosseini SM, Kelley RG, Amatya D, Hamilton JP, et al. (2013): Anomalous Gray Matter Structural Networks in Major Depressive Disorder. *Biological psychiatry*.

117. Li L, Rilling JK, Preuss TM, Glasser MF, Damen FW, Hu X (2012): Quantitative assessment of a framework for creating anatomical brain networks via global tractography. *NeuroImage*. 61:1017-1030.

118. Achard S, Bullmore E (2007): Efficiency and cost of economical brain functional networks. *PLoS computational biology*. 3:e17.

119. Kaiser M (2011): A tutorial in connectome analysis: topological and spatial features of brain networks. *NeuroImage*. 57:892-907.

120. Watts DJ, Strogatz SH (1998): Collective dynamics of 'small-world' networks. *Nature*. 393:440-442.

121. Achard S, Salvador R, Whitcher B, Suckling J, Bullmore E (2006): A resilient, low-frequency, small-world human brain functional network with highly connected association cortical hubs. *The Journal of neuroscience : the official journal of the Society for Neuroscience*. 26:63-72.

122. Iturria-Medina Y (2013): Anatomical brain networks on the prediction of abnormal brain states. *Brain connectivity*. 3:1-21.

123. Cao Q, Shu N, An L, Wang P, Sun L, Xia MR, et al. (2013): Probabilistic diffusion tractography and graph theory analysis reveal abnormal white matter structural connectivity networks in drug-naive boys with attention deficit/hyperactivity disorder. *The Journal of neuroscience : the official journal of the Society for Neuroscience*. 33:10676-10687.

124. Li L, Hu X, Preuss TM, Glasser MF, Damen FW, Qiu Y, et al. (2013): Mapping putative hubs in human, chimpanzee and rhesus macaque connectomes via diffusion tractography. *NeuroImage*. 80:462-474.

125. Liu B, Chen J, Wang J, Liu X, Duan X, Shang X, et al. (2012): Altered small-world efficiency of brain functional networks in acupuncture at ST36: a functional MRI study. *PloS one*. 7:e39342.

126. Felleman DJ, Van Essen DC (1991): Distributed hierarchical processing in the primate cerebral cortex. *Cerebral cortex*. 1:1-47.

127. Young MP (1993): The organization of neural systems in the primate cerebral cortex. *Proceedings Biological sciences / The Royal Society*. 252:13-18.

128. Li L, Rilling JK, Preuss TM, Glasser MF, Hu X (2012): The effects of connection reconstruction method on the interregional connectivity of brain networks via diffusion tractography. *Human brain mapping*. 33:1894-1913.

129. Latora V, Marchiori M (2001): Efficient behavior of small-world networks. *Physical review letters*. 87:198701.

130. Sheline YI, Barch DM, Price JL, Rundle MM, Vaishnavi SN, Snyder AZ, et al. (2009): The default mode network and self-referential processes in depression. *Proceedings of the National Academy of Sciences of the United States of America*. 106:1942-1947.

131. Walter M, Henning A, Grimm S, Schulte RF, Beck J, Dydak U, et al. (2009): The relationship between aberrant neuronal activation in the pregenual anterior cingulate, altered glutamatergic metabolism, and anhedonia in major depression. *Archives of general psychiatry*. 66:478-486.

132. Holmes AJ, Pizzagalli DA (2008): Response conflict and frontocingulate dysfunction in unmedicated participants with major depression. *Neuropsychologia*. 46:2904-2913.

133. Pizzagalli DA (2011): Frontocingulate dysfunction in depression: toward biomarkers of treatment response. *Neuropsychopharmacology : official publication of the American College of Neuropsychopharmacology*. 36:183-206.

134. Mayberg HS, Brannan SK, Mahurin RK, Jerabek PA, Brickman JS, Tekell JL, et al. (1997): Cingulate function in depression: a potential predictor of treatment response. *Neuroreport*. 8:1057-1061.

135. Davidson RJ, Pizzagalli D, Nitschke JB, Putnam K (2002): Depression: perspectives from affective neuroscience. *Annual review of psychology*. 53:545-574.

136. Holmes AJ, Pizzagalli DA (2008): Spatiotemporal dynamics of error processing dysfunctions in major depressive disorder. *Archives of general psychiatry*. 65:179-188.

137. Siegle GJ, Thompson W, Carter CS, Steinhauer SR, Thase ME (2007): Increased amygdala and decreased dorsolateral prefrontal BOLD responses in unipolar depression: related and independent features. *Biological psychiatry*. 61:198-209.

138. Aizenstein HJ, Butters MA, Wu M, Mazurkewicz LM, Stenger VA, Gianaros PJ, et al. (2009): Altered functioning of the executive control circuit in late-life depression: episodic and persistent phenomena. *The American journal of geriatric psychiatry : official journal of the American Association for Geriatric Psychiatry*. 17:30-42.

139. Schlosser RG, Wagner G, Koch K, Dahnke R, Reichenbach JR, Sauer H (2008): Fronto-cingulate effective connectivity in major depression: a study with fMRI and dynamic causal modeling. *NeuroImage*. 43:645-655.

140. Mayberg HS, Lewis PJ, Regenold W, Wagner HN, Jr. (1994): Paralimbic hypoperfusion in unipolar depression. *Journal of nuclear medicine : official publication, Society of Nuclear Medicine*. 35:929-934.

141. Bluhm R, Williamson P, Lanius R, Theberge J, Densmore M, Bartha R, et al. (2009): Resting state default-mode network connectivity in early depression using a seed region-of-interest analysis: decreased connectivity with caudate nucleus. *Psychiatry and clinical neurosciences*. 63:754-761.

142. Wagner G, Koch K, Schachtzabel C, Schultz CC, Sauer H, Schlosser RG (2011): Structural brain alterations in patients with major depressive disorder and high risk for suicide: evidence for a distinct neurobiological entity? *NeuroImage*. 54:1607-1614.

143. Muller VI, Cieslik EC, Kellermann TS, Eickhoff SB (2013): Crossmodal emotional integration in major depression. *Social cognitive and affective neuroscience*.

144. Mayberg HS, Brannan SK, Tekell JL, Silva JA, Mahurin RK, McGinnis S, et al. (2000): Regional metabolic effects of fluoxetine in major depression: serial changes and relationship to clinical response. *Biological psychiatry*. 48:830-843.

145. Goldapple K, Segal Z, Garson C, Lau M, Bieling P, Kennedy S, et al. (2004): Modulation of cortical-limbic pathways in major depression: treatment-specific effects of cognitive behavior therapy. *Archives of general psychiatry*. 61:34-41.

146. Nobler MS, Oquendo MA, Kegeles LS, Malone KM, Campbell CC, Sackeim HA, et al. (2001): Decreased regional brain metabolism after ect. *The American journal of psychiatry*. 158:305-308.

147. Bewernick BH, Hurlemann R, Matusch A, Kayser S, Grubert C, Hadrysiewicz B, et al. (2010): Nucleus accumbens deep brain stimulation decreases ratings of depression and anxiety in treatment-resistant depression. *Biological psychiatry*. 67:110-116.

148. Sartorius A, Henn FA (2007): Deep brain stimulation of the lateral habenula in treatment resistant major depression. *Medical hypotheses*. 69:1305-1308.

149. Jimenez F, Velasco F, Salin-Pascual R, Hernandez JA, Velasco M, Criales JL, et al. (2005): A patient with a resistant major depression disorder treated with deep brain stimulation in the inferior thalamic peduncle. *Neurosurgery*. 57:585-593; discussion 585-593.

150. Schlaepfer TE, Bewernick BH, Kayser S, Madler B, Coenen VA (2013): Rapid effects of deep brain stimulation for treatment-resistant major depression. *Biological psychiatry*. 73:1204-1212.

151. Lozano AM, Giacobbe P, Hamani C, Rizvi SJ, Kennedy SH, Kolivakis TT, et al. (2012): A multicenter pilot study of subcallosal cingulate area deep brain stimulation for treatment-resistant depression. *Journal of neurosurgery*. 116:315-322.

152. Puigdemont D, Perez-Egea R, Portella MJ, Molet J, de Diego-Adelino J, Gironell A, et al. (2011): Deep brain stimulation of the subcallosal cingulate gyrus: further evidence in treatment-resistant major depression. *The international journal of neuropsychopharmacology / official scientific journal of the Collegium Internationale Neuropsychopharmacologicum*.1-13.

153. Ramasubbu R, Anderson S, Haffenden A, Chavda S, Kiss ZH (2013): Double-blind optimization of subcallosal cingulate deep brain stimulation for treatment-resistant depression: a pilot study. *Journal of psychiatry & neuroscience : JPN*. 38:120160.

154. Guinjoan SM, Mayberg HS, Costanzo EY, Fahrer RD, Tenca E, Antico J, et al. (2010): Asymmetrical contribution of brain structures to treatment-resistant depression as illustrated by effects of right subgenual cingulum stimulation. *The Journal of neuropsychiatry and clinical neurosciences*. 22:265-277.

155. Kennedy SH, Giacobbe P, Rizvi SJ, Placenza FM, Nishikawa Y, Mayberg HS, et al. (2011): Deep brain stimulation for treatment-resistant depression: follow-up after 3 to 6 years. *The American journal of psychiatry*. 168:502-510.

156. Mayberg HS (1997): Limbic-cortical dysregulation: a proposed model of depression. *The Journal of neuropsychiatry and clinical neurosciences*. 9:471-481.

157. Freedman LJ, Insel TR, Smith Y (2000): Subcortical projections of area 25 (subgenual cortex) of the macaque monkey. *The Journal of comparative neurology*. 421:172-188.

158. Ongur D, Price JL (2000): The organization of networks within the orbital and medial prefrontal cortex of rats, monkeys and humans. *Cerebral cortex*. 10:206-219.

159. Carmichael ST, Price JL (1996): Connectional networks within the orbital and medial prefrontal cortex of macaque monkeys. *The Journal of comparative neurology*. 371:179-207.

160. Haber SN, Fudge JL, McFarland NR (2000): Striatonigrostriatal pathways in primates form an ascending spiral from the shell to the dorsolateral striatum. *The Journal of neuroscience : the official journal of the Society for Neuroscience*. 20:2369-2382.

161. Ghashghaei HT, Hilgetag CC, Barbas H (2007): Sequence of information processing for emotions based on the anatomic dialogue between prefrontal cortex and amygdala. *NeuroImage*. 34:905-923.

162. Schaltenbrand GW, W.; Walker, E.A. (1998): *Atlas for Stereotaxy of the Human Brain*. 2 ed.: Thieme.

163. Hamani C, Mayberg H, Snyder B, Giacobbe P, Kennedy S, Lozano AM (2009): Deep brain stimulation of the subcallosal cingulate gyrus for depression: anatomical location of active contacts in clinical responders and a suggested guideline for targeting. *Journal of neurosurgery*. 111:1209-1215.

164. Jbabdi S, Johansen-Berg H (2011): Tractography: where do we go from here? *Brain connectivity*. 1:169-183.

165. Le Bihan D, Johansen-Berg H (2012): Diffusion MRI at 25: exploring brain tissue structure and function. *NeuroImage*. 61:324-341.

166. Dostrovsky JO, Lozano AM (2002): Mechanisms of deep brain stimulation. *Movement disorders : official journal of the Movement Disorder Society*. 17 Suppl 3:S63-68.

167. Dzirasa K, Lisanby SH (2012): How does deep brain stimulation work? *Biological psychiatry*. 72:892-894.

168. Vitek JL (2002): Mechanisms of deep brain stimulation: excitation or inhibition. *Movement disorders : official journal of the Movement Disorder Society*. 17 Suppl 3:S69-72.

169. McIntyre CC, Miocinovic S, Butson CR (2007): Computational analysis of deep brain stimulation. *Expert review of medical devices*. 4:615-622.

170. Gradinaru V, Mogri M, Thompson KR, Henderson JM, Deisseroth K (2009): Optical deconstruction of parkinsonian neural circuitry. *Science*. 324:354-359.

171. Follett KA, Weaver FM, Stern M, Hur K, Harris CL, Luo P, et al. (2010): Pallidal versus subthalamic deep-brain stimulation for Parkinson's disease. *The New England journal of medicine*. 362:2077-2091.

172. Whitmer D, de Solages C, Hill B, Yu H, Henderson JM, Bronte-Stewart H (2012): High frequency deep brain stimulation attenuates subthalamic and cortical rhythms in Parkinson's disease. *Frontiers in human neuroscience*. 6:155.

173. Butson CR, Cooper SE, Henderson JM, Wolgamuth B, McIntyre CC (2011): Probabilistic analysis of activation volumes generated during deep brain stimulation. *NeuroImage*. 54:2096-2104.

174. Butson CR, Cooper SE, Henderson JM, McIntyre CC (2007): Patient-specific analysis of the volume of tissue activated during deep brain stimulation. *NeuroImage*. 34:661-670.

175. Little S, Pogosyan A, Neal S, Zavala B, Zrinzo L, Hariz M, et al. (2013): Adaptive deep brain stimulation in advanced Parkinson disease. *Annals of neurology*.

176. Iacono RP, Lonser RR, Maeda G, Kuniyoshi S, Warner D, Mandybur G, et al. (1995): Chronic anterior pallidal stimulation for Parkinson's disease. *Acta neurochirurgica*. 137:106-112.

177. Charles PD, Padaliya BB, Newman WJ, Gill CE, Covington CD, Fang JY, et al. (2004): Deep brain stimulation of the subthalamic nucleus reduces antiparkinsonian medication costs. *Parkinsonism & related disorders*. 10:475-479.

178. Mori Y, Shiota T, Jones M, Wanitkun S, Irvine T, Li X, et al. (1999): Three-dimensional reconstruction of the color Doppler-imaged vena contracta for quantifying aortic regurgitation: studies in a chronic animal model. *Circulation*. 99:1611-1617.

179. Jones DK, Simmons A, Williams SC, Horsfield MA (1999): Non-invasive assessment of axonal fiber connectivity in the human brain via diffusion tensor MRI. *Magnetic resonance in medicine : official journal of the Society of Magnetic Resonance in Medicine / Society of Magnetic Resonance in Medicine*. 42:37-41.

180. Conturo TE, Lori NF, Cull TS, Akbudak E, Snyder AZ, Shimony JS, et al. (1999): Tracking neuronal fiber pathways in the living human brain. *Proceedings of the National Academy of Sciences of the United States of America*. 96:10422-10427.

181. Parker GJM, Wheeler-Kingshott CAM, Barker GJ (2002): Estimating distributed anatomical connectivity using fast marching methods and diffusion tensor Imaging. *IEEE transactions on medical imaging*. 21:505-512.

182. Mori S, van Zijl PC (2002): Fiber tracking: principles and strategies - a technical review. *NMR in biomedicine*. 15:468-480.

183. Wakana S, Jiang H, Nagae-Poetscher LM, van Zijl PC, Mori S (2004): Fiber tract-based atlas of human white matter anatomy. *Radiology*. 230:77-87.

184. Parker GJ, Alexander DC (2005): Probabilistic anatomical connectivity derived from the microscopic persistent angular structure of cerebral tissue. *Philosophical transactions of the Royal Society of London Series B, Biological sciences*. 360:893-902.

185. Behrens TE, Berg HJ, Jbabdi S, Rushworth MF, Woolrich MW (2007): Probabilistic diffusion tractography with multiple fibre orientations: What can we gain? *NeuroImage*. 34:144-155.

186. Bhatia KD, Henderson L, Ramsey-Stewart G, May J (2012): Diffusion tensor imaging to aid subgenual cingulum target selection for deep brain stimulation in depression. *Stereotactic and functional neurosurgery*. 90:225-232.

187. Lehman JF, Greenberg BD, McIntyre CC, Rasmussen SA, Haber SN (2011): Rules ventral prefrontal cortical axons use to reach their targets: implications for diffusion tensor imaging tractography and deep brain stimulation for psychiatric illness. *The Journal of neuroscience : the official journal of the Society for Neuroscience*. 31:10392-10402.

188. Chaturvedi A, Lujan J, McIntyre C (2013): Artificial neural network based characterization of the volume of tissue activated during deep brain stimulation. *Journal of Neural Engineering*. 10:in press.

189. Frankemolle AM, Wu J, Noecker AM, Voelcker-Rehage C, Ho JC, Vitek JL, et al. (2010): Reversing cognitive-motor impairments in Parkinson's disease patients using a computational modelling approach to deep brain stimulation programming. *Brain : a journal of neurology*. 133:746-761.

190. Lujan JL, Chaturvedi A, Choi KS, Holtzheimer PE, Gross RE, Mayberg HS, et al. (2013): Tractography-Activation Models Applied to Subcallosal Cingulate Deep Brain Stimulation. *Brain stimulation*.

191. Hamilton M (1960): A rating scale for depression. *Journal of neurology, neurosurgery, and psychiatry*. 23:56-62.

192. Ashutosh Chaturvedi JLL, Cameron C. McIntyre (2013): Artificial neural network based characterization of the volume of tissue activated during deep brain stimulation. *IOP*.

193. Jenkinson M, Beckmann CF, Behrens TE, Woolrich MW, Smith SM (2012): Fsl. *NeuroImage*. 62:782-790.

194. Behrens TE, Johansen-Berg H, Woolrich MW, Smith SM, Wheeler-Kingshott CA, Boulby PA, et al. (2003): Non-invasive mapping of connections between human thalamus and cortex using diffusion imaging. *Nature neuroscience*. 6:750-757.

195. Desikan RS, Segonne F, Fischl B, Quinn BT, Dickerson BC, Blacker D, et al. (2006): An automated labeling system for subdividing the human cerebral cortex on MRI scans into gyral based regions of interest. *NeuroImage*. 31:968-980.

196. Fischl B, Sereno MI, Dale AM (1999): Cortical surface-based analysis. II: Inflation, flattening, and a surface-based coordinate system. *NeuroImage*. 9:195-207.

197. Makris N, Goldstein JM, Kennedy D, Hodge SM, Caviness VS, Faraone SV, et al. (2006): Decreased volume of left and total anterior insular lobule in schizophrenia. *Schizophrenia research*. 83:155-171.

198. Frazier JA, Chiu S, Breeze JL, Makris N, Lange N, Kennedy DN, et al. (2005): Structural brain magnetic resonance imaging of limbic and thalamic volumes in pediatric bipolar disorder. *The American journal of psychiatry*. 162:1256-1265.

199. Goldstein JM, Seidman LJ, Makris N, Ahern T, O'Brien LM, Caviness VS, Jr., et al. (2007): Hypothalamic abnormalities in schizophrenia: sex effects and genetic vulnerability. *Biological psychiatry*. 61:935-945.

200. Kelley ME, Franco AR, Mayberg HS, Holtzheimer PE (2012): The Illness Density Index (IDI): A longitudinal measure of treatment efficacy. *Clinical trials*. 9:596-604.

201. Setsompop K, Kimmlingen R, Eberlein E, Witzel T, Cohen-Adad J, McNab JA, et al. (2013): Pushing the limits of in vivo diffusion MRI for the Human Connectome Project. *NeuroImage*. 80:220-233.

202. Martens HC, Toader E, Decre MM, Anderson DJ, Vetter R, Kipke DR, et al. (2011): Spatial steering of deep brain stimulation volumes using a novel lead design. *Clinical neurophysiology : official journal of the International Federation of Clinical Neurophysiology*. 122:558-566.

203. Tawfik VL, Chang SY, Hitti FL, Roberts DW, Leiter JC, Jovanovic S, et al. (2010): Deep brain stimulation results in local glutamate and adenosine release: investigation into the role of astrocytes. *Neurosurgery*. 67:367-375.

204. Hamani C, Nobrega JN (2012): Preclinical studies modeling deep brain stimulation for depression. *Biological psychiatry*. 72:916-923.